arXiv:2502.20403v2 [cs.ET] 6 Mar 2026

Adversarial Robustness of Partitioned Quantum Classifiers

Pouya Kananian and Hans-Arno Jacobsen

Department of Electrical and Computer Engineering, University of Toronto, Toronto, Canada

pouya.kananian@mail.utoronto.ca, jacobsen@eecg.toronto.edu

Abstract

Adversarial robustness in quantum classifiers is a critical area of study, providing insights into their performance compared to classical models and uncovering potential advantages inherent to quantum machine learning. In the NISQ era of quantum computing, circuit cutting is a notable technique for simulating circuits that exceed the qubit limitations of current devices, enabling the distribution of a quantum circuit's execution across multiple quantum processing units through classical communication. In contrast, when quantum communication is available, teleportation-based methods can be used to support the distribution of the quantum circuit. We study the robustness of partitioned quantum classifiers to adversarial perturbations targeting wire cutting or quantum state teleportation and show a link between such perturbations and implementing adversarial gates within intermediate layers of a quantum classifier. We then proceed to study the latter problem from both a theoretical and experimental perspective.

1 Introduction

Quantum machine learning (QML) has emerged as a thriving and rapidly evolving field of study (Biamonte et al., 2017; Abbas et al., 2021; Liu et al., 2021; Cerezo et al., 2022; Larocca et al., 2024). Especially, variational quantum classifiers hold particular significance due to their practical applications in the Noisy Intermediate-Scale Quantum (NISQ) era of quantum computing (Cerezo et al., 2021; Bharti et al., 2022). An increasingly important domain in QML that has captured attention recently is adversarial robustness of quantum classifiers (Lu et al., 2020; Liu and Wittek, 2020; Du et al., 2021; Weber et al., 2021; Liao et al., 2021; Gong et al., 2022; Gong and Deng, 2022; Anil et al., 2024; Dowling et al., 2024). This area is vital for comparing the performance of quantum classifiers against classical models and exploring the potential advantages within QML (West et al., 2023b).

Current NISQ era quantum devices feature a small number of noisy qubits. To address the limited qubit count in these devices, numerous methods (Bravyi et al., 2016; Peng et al., 2020; Yuan et al., 2021; Mitarai and Fujii, 2021a;b; Fujii et al., 2022; Eddins et al., 2022) have been suggested to expand the size of quantum systems through the use of classical processing. A notable category of such approaches, known as circuit cutting (Lowe et al., 2023) or circuit knitting (Piveteau and Sutter, 2023), involves partitioning quantum circuits into smaller fragments that can be executed on devices with fewer qubits than required by the original circuit. After execution, classical post-processing can be employed to combine the measurement outcomes and simulate quantum circuits that surpass the qubit limitations of a given device. Most circuit cutting approaches are primarily based on quasiprobability simulation, a commonly employed technique in quantum error mitigation (Temme et al., 2017; Endo et al., 2018; Piveteau et al., 2022) and classical simulation of quantum systems (Pashayan et al., 2015; Howard and Campbell, 2017; Seddon and Campbell, 2019; Seddon et al., 2021). Quantum channels describe the evolution of quantum states, with the identity channel mapping a quantum state to itself. Quasiprobability decomposition allows us to decompose the identity channel into a linear combination of measurement and state-preparation channels. Similarly, it can break down a non-local channel into a sum of tensor products of local channels. This process is known as wire cutting (Peng et al., 2020; Uchehara et al., 2022; Lowe et al., 2023; Pednault, 2023; Brenner et al., 2023; Harada et al., 2024; Harrow and Lowe, 2024) when applied to the identity channel and gate cutting (Mitarai and Fujii, 2021a;b; Piveteau and Sutter, 2023; Schmitt et al., 2023; Ufrecht et al., 2023; 2024; Harrow and Lowe, 2024) when applied to non-local channels.

Quantum teleportation (Bennett et al., 1993; Ren et al., 2017) is a key method in quantum communication that allows the transmission of an unknown quantum state using shared entanglement and classical communication (Cuomo et al., 2020; Cacciapuoti et al., 2020). In the absence of quantum communication, circuit cutting can be employed to distribute the execution of a quantum circuit across multiple quantum processing units, combining quantum and classical computational resources (Barral et al., 2024). Conversely, when quantum communication is available, teleportation-based methods (Bennett et al., 1993; Bouwmeester et al., 1997; Boschi et al., 1998; Narottama and Shin, 2023) can be employed to distribute quantum circuits across nodes. While circuit cutting leads to an exponential sampling overhead, quantum telepor-

tation does not; however, it consumes entangled qubit pairs shared between the parties.

This paper focuses on how distributing a quantum classifier's circuit through circuit cutting or teleportation-based methods can inadvertently increase its exposure to adversarial attacks. When a model is distributed across multiple processors, each device is exposed to the risk of tampering by malicious inputs or compromised participants. If an adversary manipulates the subcircuits created through circuit cutting in any way, combining their outcomes may no longer reproduce the output of the original circuit that was meant to be simulated. This also holds true when teleportation-based methods are used for distributing the circuit. However, adversarial robustness of partitioned quantum classifiers has not, to the best of our knowledge, been previously studied, highlighting a crucial gap in the distributed QML literature.

One possible method of manipulating the subcircuits is through adversarial perturbations, which denote small alterations to the input states of classifiers, designed to deceive the models into making inaccurate predictions (Szegedy et al., 2013). Unlike gate cutting, wire cutting involves preparing new states for the circuit fragments created through circuit cutting. As a result, the subcircuits' input states are either retained from the original circuit or are prepared as part of wire cutting. In Section 4, we examine how adding adversarial perturbations to the prepared states in wire cutting, instead of manipulating the classifier's input states, enables an adversary to plant adversarial gates within intermediate layers of the simulated circuit, constructed by merging the results of the circuit fragments (see Fig. 1). Similarly, as discussed in Section 5, when quantum state teleportation is used to distribute the circuit, introducing carefully crafted adversarial perturbations before teleporting an state or after receiving it may be viewed as inserting adversarial gates within intermediate layers of the original circuit. The connection between adversarial attacks targeting the wire cutting procedure and those manipulating the state teleporation method with insertion of adversarial gates within a quantum classifier's architecture motivates us to study the latter problem. In Section 6, we present theorems bounding the potential variation implementing multiple adversarial gates within intermediate layers of a quantum classifier could cause in its predictive confidence. Section 7 experimentally investigates the impact of planting one or more global or local adversarial gates at different depths of variational quantum classifiers. It also provides an experimental evaluation of our theoretical bounds.

2 Related Work

2.1 Adversarial Robustness of Quantum Classifiers

There is a rich body of literature that studies the adversarial robustness of quantum classifiers, both theoretically (Liu and Wittek, 2020; Liao et al., 2021; Weber et al., 2021; Guan et al., 2021; Du et al., 2021; Gong and Deng, 2022; Anil et al., 2024; Dowling et al., 2024) and experimentally (Lu et al., 2020; Ren et al., 2022; West et al., 2023a). Although the intersection of circuit cutting and QML has garnered some attention in recent years (Pira and Ferrie, 2023; Guala et al., 2023; Marshall et al., 2023; Marchisio et al., 2024; Sahu and Gupta, 2024), to the best of our knowledge, this is the first study to explore the impact of partitioning quantum classifier through circuit cutting on their adversarial robustness. Adversarial robustness in quantum federated learning has been extensively studied (Li et al., 2021; Xia et al., 2021; Zhang et al., 2022; Kumar et al., 2023; Chu et al., 2023; Li et al., 2024a; Chen et al., 2024; Papadopoulos et al., 2025; Maouaki et al., 2025). The distribution approach in these federated learning works, however, is fundamentally different from the circuit distribution techniques based on circuit cutting. Federated learning (Konečný et al., 2016a;b; McMahan et al., 2017) allows multiple participants to collaboratively train a shared model without sharing their local private data. Quantum computing can be incorporated into federated learning through quantum data (Xia and Li, 2021; Chehimi and Saad, 2022), QML models (Huang et al., 2022; Kumar et al., 2023), or quantum communication (Li et al., 2021; Zhang et al., 2022; Xu et al., 2023). However, unlike classical computing, which benefits from widely available hardware like IoT devices, smartphones, and edge servers for federated training, quantum computing lacks this flexibility due to its limited and costly hardware. It is therefore imperative to study the distributed execution of a single quantum model across multiple quantum processors, as well as to investigate the adversarial robustness of such distributed models.

Several prior studies have examined quantum teleportation in adversarial settings in the context of secure communication (Ahlswede et al., 2013; Hamdoun and Sagheer, 2020; Tserkis et al., 2020; Kumar and Garhwal, 2021; Gangopadhyay et al., 2022; Nang Paing et al., 2022; Unnikrishnan and Markham, 2020; Bajpayee et al., 2024; Huang et al., 2024; Holmes, 2025; Rahmawati et al., 2025; Neves et al., 2025). In contrast, we explore a novel adversarial scenario that focuses on the performance of a quantum classifier. We assume ideal quantum teleportation, in which the teleportation channel acts as the identity channel on the teleported state with unit fidelity. Nevertheless, the state may be manipulated through the introduction of adversarial perturbations either prior to transmission or after it is received. This scenario, which is similar to those studied in classical split learning (see Section 2.2), is connected to the adversarial case we analyze for wire cutting. In both settings, introducing adversarial perturbations to the identity channel implemented through wire cutting or state teleportation results in the incorporation of adversarial gates within the intermediate layers of the circuit. Our attack model, outlined in Section 3.4, provides a more general framework for understanding the implications of implementing adversarial gates within a quantum classifier's architecture, extending beyond those previous works that focus only on adversarial perturbations targeting the input state

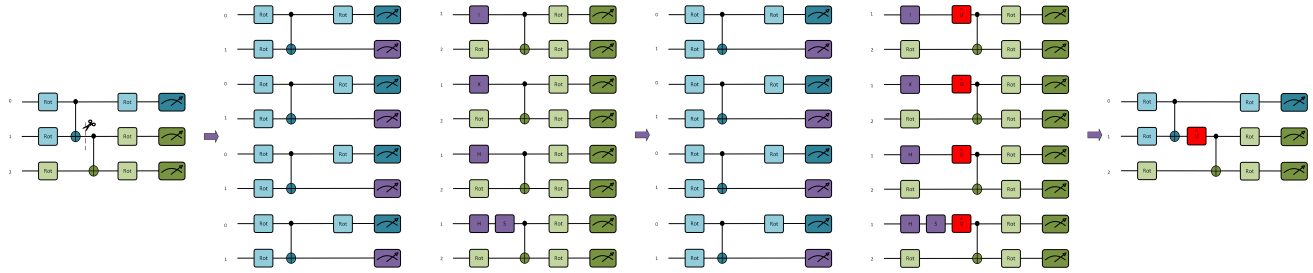

Figure 1: Wire cutting applied to a simple quantum circuit, decomposing it into multiple sub-circuits. In the resulting sub-circuits, the cut wire from the original circuit is replaced by measurement and state preparation channels, shown in purple. The input states of the green sub-circuits are adversarially modified through the application of a perturbation gate $\hat{U}$. When the results of the sub-circuits are recombined to reconstruct the original circuit, this adversarial attack leads to the insertion of $\hat{U}$ in the intermediate layers of the reconstructed circuit.

(Liao et al., 2021; Dowling et al., 2024).

Du et al. (2021) show that the depolarization noise present in NISQ-era quantum classifiers can make them inherently quantum differentially private (Dwork et al., 2006; Zhou and Ying, 2017) and naturally resilient to adversaries (Cohen et al., 2019). Numerous methods (Watkins et al., 2023; Huang et al., 2023; Huang and Zhang, 2023; Winderl et al., 2024; Khatun and Usman, 2025a) have been proposed to improve the adversarial robustness of quantum classifiers, including adversarial training (Lu et al., 2020; Ren et al., 2022; Khatun and Usman, 2025b; Montalbano and Banchi, 2025), as well as randomized and approximate encoding schemes (Gong et al., 2022; West et al., 2024; Wollschläger et al., 2024; Saxena et al., 2024). In this work, we focus on noise-free quantum classifiers without additional adversarial robustness enhancements, leaving the exploration of enhancement strategies to future work.

2.2 Relevant Adversarial Scenarios in Classical Systems

The adversarial scenario explored in this work bears similarities to those observed in split learning frameworks within classical machine learning (Gajbhiye et al., 2022; Fan et al., 2023; Bai et al., 2023; Yu et al., 2023; He et al., 2024; Shabbir et al., 2025). In split learning (Gupta and Raskar, 2018; Vepakomma et al., 2018; Gao et al., 2020), the model is segmented into sub-networks executed by separate participants to facilitate collaborative training. Raw data remains on the client's device, with only intermediate results communicated to the server, thereby reducing the computational demands on the client. Split learning is vulnerable to several privacy threats (Shabbir et al., 2025), including inference (Pasquini et al., 2021; Fu et al., 2022), reconstruction (Gawron and Stubbings, 2022; Mao et al., 2023), and model inversion (Erdoğan et al., 2022) attacks, as well as adversarial attacks such as evasion (Fan et al., 2023; He et al., 2024) and poisoning (Bai et al., 2023; Yu et al., 2024). An untrusted server in split learning may tamper with the inputs or outputs of its assigned layers or collect data to train proxy models (Fan et al., 2023). One possible adversarial scenario involves generating adversarial examples by manipulating the intermediate outputs of the model (Fan et al., 2023; He et al., 2024). Although this scenario is relevant to our work, the machine learning models and partitioning approaches in quantum computing differ from those in classical systems, making it essential to conduct a separate study.

2.3 Wire Cutting and Quantum Teleportation

Circuit cutting has attracted growing interest and attention from researchers in recent years (Tang et al., 2021; Majumdar and Wood, 2022; Liu et al., 2022; Casciola et al., 2022; Chen et al., 2022; 2023a;b; Brandhofer et al., 2023; Nagai et al., 2023; Pérez-Salinas et al., 2023; Bhoumik et al., 2023; Seitz et al., 2024; Gentinetta et al., 2024; Li et al., 2024b). In this work, we specifically focus on wire cutting. This is because cutting wires, in contrast to cutting gates, involves measuring qubits, transforming quantum information into classical information, and preparing new quantum states. Studying the robustness of quantum classifiers to adversarial perturbations targeting these new states can be viewed as a natural generalization of studying their robustness to adversarial attacks targeting their input states.

Multiple studies have focused on improving the original wire cutting decomposition (Peng et al., 2020) to reduce sampling overhead and minimize the number of channels needed for cutting multiple wires (Brenner et al., 2023; Lowe et al., 2023; Pednault, 2023; Harada et al., 2024; Harrow and Lowe, 2024). To study the adversarial robustness of quantum classifiers that undergo wire cutting, we primarily focus on the original wire cutting decomposition (Peng et al., 2020) and the decomposition proposed by Harada et al. (2024), which achieves the optimal sampling overhead and number of channels required for cutting parallel wires. However, other wire cutting approaches based on measure-and-prepare channels could be vulnerable to similar attacks addressed in this paper. A range of works has investigated finding optimal cut locations and intelligent strategies for qubit assignment across processors (Tang et al., 2021; Tang and Martonosi, 2022; Smith et al., 2023; Brandhofer et al., 2023). Similarly,

when quantum teleportation is used for distributing circuits, minimizing the e-bit cost as well as optimizing partitioning strategies are widely studied (Zomorodi-Moghadam et al., 2018; Heunen and Martinez, 2019; Houshmand et al., 2020; Baker et al., 2020; G Sundaram et al., 2021; Nikahd et al., 2021; Ferrari et al., 2021; 2023; Cuomo et al., 2023). Our study applies to distributed classifiers, regardless of where their circuits are partitioned.

3 Preliminaries

Here, we review key notations and distance metrics, provide a brief overview of quantum classification, wire cutting, and state teleportation, and introduce our attack model.

3.1 Quantum Channels and Diamond Distance

A linear map $\mathcal{M} : \mathcal{L}(\mathcal{H}_A) \to \mathcal{L}(\mathcal{H}_B)$ is called trace-preserving (TP) if $\text{Tr}(\mathcal{M}(X)) = \text{Tr}(X)$ for all $X \in \mathcal{L}(\mathcal{H}_A)$, where $\mathcal{H}_A$ and $\mathcal{H}_B$ are Hilbert spaces and $\mathcal{L}(\mathcal{H})$ represents the space of square linear operators acting on the Hilbert space $\mathcal{H}$. A linear map $\mathcal{M} : \mathcal{L}(\mathcal{H}_A) \to \mathcal{L}(\mathcal{H}_B)$ is completely positive (CP) if for a reference system R of arbitrary size, $(\mathcal{I}_R \otimes \mathcal{M})(X)$ is positive semi-definite for all positive semi-definite $X \in \mathcal{L}(\mathcal{H}_R \otimes \mathcal{H}_A)$, where $\mathcal{I}_R$ represents the identity map acting on $\mathcal{H}_R$. A quantum channel is a linear map that is both completely positive and trace-preserving (CPTP). For a linear map $\mathcal{M} : \mathcal{L}(\mathcal{H}_A) \to \mathcal{L}(\mathcal{H}_B)$, the adjoint of this map $\mathcal{M}^\dagger : \mathcal{L}(\mathcal{H}_B) \to \mathcal{L}(\mathcal{H}_A)$ is the unique linear map satisfying $\langle A, \mathcal{M}(B)\rangle = \langle \mathcal{M}^\dagger(A), B\rangle$ for all $A \in \mathcal{L}(\mathcal{H}_A)$ and $B \in \mathcal{L}(\mathcal{H}_B)$, where $\langle A, B\rangle := \text{Tr}[A^\dagger B]$ denotes the Hilbert–Schmidt inner product. The diamond distance between two quantum channels $\mathcal{N}, \mathcal{M} : \mathcal{L}(\mathcal{H}_A) \to \mathcal{L}(\mathcal{H}_B)$ is defined as

$$\|\mathcal{N} - \mathcal{M}\|_\diamond := \sup_\rho \|(\mathcal{I}_R \otimes \mathcal{N})(\rho) - (\mathcal{I}_R \otimes \mathcal{M})(\rho)\|_1,$$

where the supremum is taken over all density operators acting on $\mathcal{H}_R \otimes \mathcal{H}_A$, and $\|.\|_1$ denotes the trace norm (also known as the Schatten 1-norm).

In this paper, we use $\|.\|_2$ and $\|.\|_{op}$ to denote the Hilbert-Schmidt norm (or the Schatten 2-norm) and the largest singular value (also referred to as the operator norm or spectral norm), respectively. For $\rho \in [1, \infty)$, the Schatten ρ-norm is defined as

$$\|C\|_\rho := \left(\mathbf{Tr}\left[\left(\sqrt{C^\dagger C}\right)^\rho\right]\right)^{1/\rho},$$

where C is a linear operator taking $\mathcal{H}$ to another Hilbert space $\mathcal{H}'$.

3.2 Quantum K-multiclass Classification

The objective of K-multiclass classification is to learn a model $y(\sigma) = h(\sigma; \theta)$ that assigns a class label $k \in \{0, \cdots, K-1\}$ to each input data sample $\sigma \in S_\sigma$, where h refers to a function (or hypothesis) parameterized by θ, and S_σ denotes the set of possible input samples. Consider a training dataset $D_M = \{\sigma_i, Y(\sigma_i)\}_{i=1}^M$, with $Y(\sigma_i)$ representing a one-hot K-dimensional vector that indicates the class label of the input state σ_i. The model parameters, denoted as θ, are typically optimized during the training process to minimize the empirical risk $L_M = (1/M)\sum_{i=1}^M L(h(\sigma_i; \theta), Y(\sigma_i))$, where L represents a loss function. We use θ^* to represent the optimized parameters.

A quantum circuit can be used for obtaining $y(\sigma)$. Let $\mathcal{H}^{\otimes d}$ and $\mathcal{D}(\mathcal{H}^{\otimes d})$ denote the d-fold tensor product of the Hilbert space $\mathcal{H}$ and the set of density operators acting on $\mathcal{H}^{\otimes d}$, respectively. For a quantum state $\sigma \in S_\sigma$, where $S_\sigma \subseteq \mathcal{D}(\mathcal{H}^{\otimes d})$, we define $y_k(\sigma)$ as the probability of obtaining the measurement outcome k in the quantum circuit (Du et al., 2021).

$$y_k(\sigma) := \text{Tr}(\Pi_k \mathcal{E}(\sigma \otimes |a\rangle\langle a|)), \tag{1}$$

with Π_k representing a positive-operator valued measure (POVM), $\mathcal{E}$ a completely positive trace-preserving (CPTP) map dependent on the parameter θ^*, and $|a\rangle\langle a| \in \mathcal{D}(\mathcal{H}^{\otimes d_a})$ an ancilla state. Here, d and d_a denote the number of input and ancilla qubits, respectively. We use $d_+ := d + d_a$ to indicate the total number of qubits in the circuit. $y_k(\sigma)$ represents the probability of assigning label k to σ, with $y(\sigma) = \text{argmax}_k\, y_k(\sigma)$ denoting the class label ultimately assigned to this input sample by the learning algorithm.

3.3 Quantum Classifiers and Adversarial Attacks

An adversarial perturbation refers to a small modification to the input of a classifier, aimed at misleading the model into making incorrect predictions. Such a perturbation could be added to the input state of a quantum classifier through a unitary perturbation operator $\hat{U}$[1]. In untargeted attacks, the adversary's goal is typically to find a perturbation that maximizes the following loss (Lu et al., 2020).

$$\hat{U} = \underset{\hat{U} \in S_{adv}}{\text{argmax}}\, L(h(\hat{U}\sigma_i\hat{U}^\dagger; \theta^*), Y(\sigma_i)), \tag{2}$$

where $S_{adv} \subseteq U(2^d)$, with $U(2^d)$ denoting the set of $2^d \times 2^d$ unitary matrices. In targeted attacks, where the aim is to misclassify an input into a specific class, the optimization objective can be formulated as follows (Lu et al., 2020).

$$\hat{U} = \underset{\hat{U} \in S_{adv}}{\text{argmin}}\, L(h(\hat{U}\sigma_i\hat{U}^\dagger; \theta^*), \hat{Y}_i), \tag{3}$$

[1]More generally, the input state could be perturbed by a CPTP map. Another setup for adversarial attacks in quantum classifiers that use classical inputs encoded as quantum states, involves the adversary perturbing classical inputs prior to their encoding, rather than perturbing the quantum states through unitary operations. This paper leaves such classical perturbations outside its scope.

where $\hat{Y}_i \neq Y(\sigma_i)$. The set of perturbation operators S_{adv} often consists of unitaries close to the identity operator. Approaches to ensure proximity to the identity operator include limiting the perturbation operator to products of local unitaries close to the identity transformation (Lu et al., 2020; Gong and Deng, 2022) or adding fidelity constraints to the adversarial attacker's loss to control the strength of the perturbation (Anil et al., 2024).

3.4 Attack Model

In this paper, we consider an adversary that can not only perturb the input state but also insert adversarial gates within the intermediate layers of a quantum classifier's circuit (see Fig. 2). This attack model's connection to wire cutting and state teleportation is explored in Sections 4 and 5, respectively. In the presence of such an adversary, the probability of assigning label k to input σ will be modified to

$$\hat{y}_k(\sigma) := \mathrm{Tr}(\Pi_k \hat{\mathcal{E}}(\hat{U}_0 \sigma \hat{U}_0^\dagger \otimes |a\rangle\langle a|)), \tag{4}$$

where

$$\begin{aligned} \hat{\mathcal{E}}(.) &= \hat{U}_n(\mathcal{E}_n \cdots (\hat{U}_1(\mathcal{E}_1(.))\hat{U}_1^\dagger) \cdots)\hat{U}_n^\dagger, \\ \mathcal{E}(.) &= \mathcal{E}_n \cdots \mathcal{E}_2(\mathcal{E}_1(.)), \end{aligned} \tag{5}$$

and each perturbation operator $\hat{U}_i \in S_{adv} \subseteq U(2^d) \cup U(2^{d+})$. Alternatively, we could represent $\hat{\mathcal{E}}(.)$ as

$$\hat{\mathcal{E}}(.) = \hat{\mathcal{U}}_n \circ \mathcal{E}_n \cdots \circ \hat{\mathcal{U}}_1 \circ \mathcal{E}_1(.), \tag{6}$$

with $\hat{\mathcal{U}}_i(.) = \hat{U}_i(.)\hat{U}_i^\dagger$ denoting the unitary channel corresponding to $\hat{U}_i$. For this type of adversary, the optimization objectives in (2) and (3) can be generalized to

$$(\hat{U}_0, \hat{U}_1, \cdots, \hat{U}_n) = \underset{\hat{U}_i \in S_{adv}, \forall i}{\mathrm{argmax}} \; L(\hat{y}(\sigma_i), Y(\sigma_i)), \tag{7}$$

and

$$(\hat{U}_0, \hat{U}_1, \cdots, \hat{U}_n) = \underset{\hat{U}_i \in S_{adv}, \forall i}{\mathrm{argmin}} \; L(\hat{y}(\sigma_i), \hat{Y}_i),$$

respectively, where $\hat{y}(\sigma_i) = \mathrm{argmax}_k \, \hat{y}(\sigma_i)$.

3.5 Wire Cutting

In a quantum circuit with the objective of estimating an observable O_{out}, the expected value of O_{out} can be expressed as $\langle O_{out} \rangle = \mathrm{Tr}(O_{out}\mathcal{E}(\sigma))$, where $\mathcal{E}$ is a channel implemented by this circuit and σ denotes a d-qubit input state. The original wire cutting method introduced by Peng et al. (2020), is based on replacing identity channels with linear combinations of measurement and state preparation operations. The decomposition of a single-qubit identity channel could be expressed as

$$\mathcal{I}(\rho) = \sum_{i=1}^{8} c_i \rho_i \mathrm{Tr}(O_i \rho). \tag{8}$$

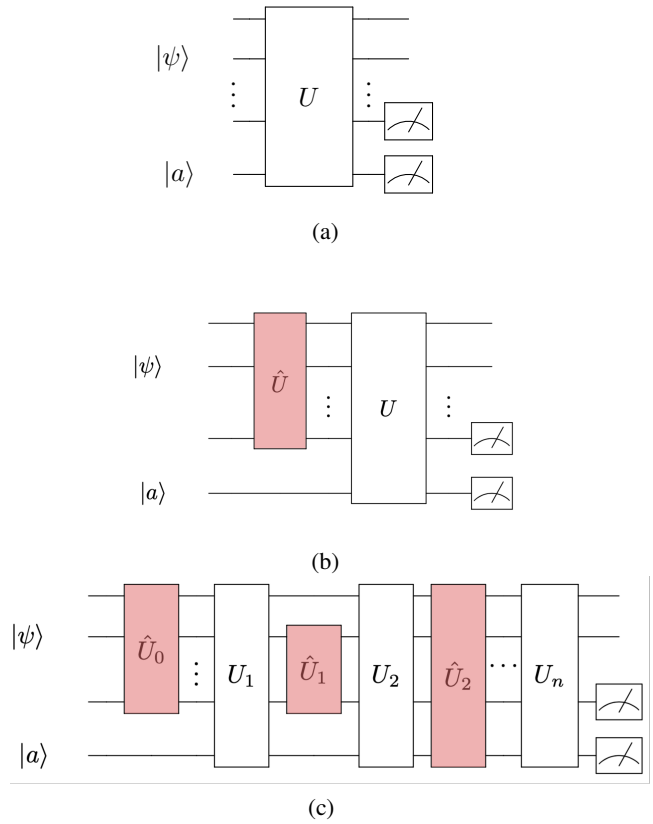

Figure 2: A Quantum classifier (a) without exposure to adversarial perturbations, (b) with an adversarial unitary gate impacting the input state, and (c) under the influence of multiple adversarial gates, highlighted in red. Here, $\sigma = |\psi\rangle\langle\psi|$ and $|a\rangle\langle a|$ denote the input and ancilla states, respectively. $U = U_n \cdots U_2 U_1$ depends on the parameter θ^* and each $\hat{U}_i \in S_{adv}$ denotes an adversarial perturbation operator. The adversarial gates may target a few local qubits or all qubits.

Here, ρ and ρ_i denote density matrices, while c_i and O_i represent a real-valued coefficient and a Hermitian observable corresponding to a measurement, respectively. Fig. 3 illustrates a simple quantum circuit partitioned using wire cutting. After cutting a wire in the circuit, the expected value of O_{out} can be expressed as:

$$\begin{aligned} \langle O_{out} \rangle =& \mathrm{Tr}(O_{out}\mathcal{E}(\sigma)) \\ =& \sum_{i=1}^{8} c_i \mathrm{Tr}\big((O_i \otimes O_{out}) \big(\mathcal{E}_{up}(\sigma_{up}) \\ & \otimes \mathcal{E}_{down}(\rho_i \otimes \sigma_{down})\big)\big), \end{aligned}$$

where $\mathcal{E}_{up}$ and $\mathcal{E}_{down}$ represent the channels implemented by the top and bottom subcircuits, respectively, while σ_{up} and σ_{down} denote marginal states of σ corresponding to $\mathcal{E}_{up}$ and $\mathcal{E}_{down}$: $\sigma = \sigma_{up} \otimes \sigma_{down}$.

Equation (8) can be extended to accommodate cutting m parallel wires, which results in the following decomposition

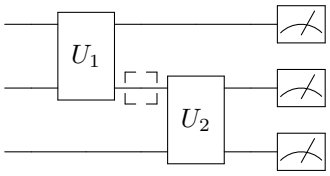

(a) Simple quantum circuit.

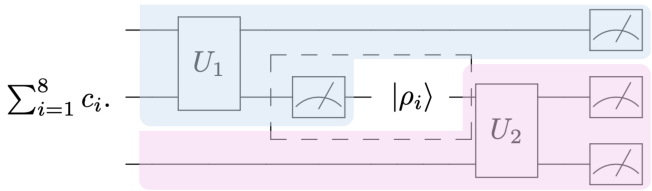

(b) The circuit after quasiprobabilistically decomposing the identity channel, highlighted by the dashed box in (a), using Equation (8).

Figure 3: Quantum circuit partitioned using wire cutting. The original circuit in (a) could be simulated by running the subcircuits in (b) and combing the results through classical post-processing.

(Harada et al., 2024) for the m-qubit identity channel.

$$\mathcal{I}^{\otimes m}(\rho) = \frac{1}{2^m} \sum_{P \in \{I,X,Y,Z\}^{\otimes m}} \mathrm{Tr}[P\rho]P, \tag{9}$$

where P denotes an $m-$qubit Pauli string, and each term $\mathrm{Tr}[P(.)]P$ can be interpreted as measuring the expectation value of P and subsequently feeding the eigenstates of P into the following subcircuit. More efficient decomposition methods for cutting $m-$parallel wires have been proposed (Lowe et al., 2023; Brenner et al., 2023; Pednault, 2023; Harada et al., 2024; Harrow and Lowe, 2024). For instance, the approach proposed by Harada et al. (2024), achieves optimal sampling overhead and minimizes the number of channels required for cutting parallel wires. This decomposition is based on removing the redundancy in the number of channels in (9) by jointly diagonalizing the Pauli strings using mutually unbiased bases (Wootters and Fields, 1989; Lawrence et al., 2002; Seyfarth, 2019; Gokhale et al., 2020). The $4^m - 1$ Pauli strings $\{I, X, Y, Z\}^{\otimes m} \backslash I^{\otimes m}$ in (9) could be partitioned into $2^m + 1$ disjoint sets $\{S_i\}_{i=1}^{2^m+1}$, with each set including $2^m - 1$ mutually commuting Pauli strings (Lawrence et al., 2002). This is due to the existence of $2^m + 1$ distinct orthonormal bases within an m-qubit system that are mutually unbiased (Wootters and Fields, 1989). Using this partitioning, we get the following decomposition, which reduces the cardinality of the sum compared to (9).

$$\mathcal{I}^{\otimes m}(\rho) = \frac{1}{2^m}\mathrm{Tr}[I^{\otimes m}\rho]I^{\otimes m} + \frac{1}{2^m}\sum_{i=1}^{2^m+1}\sum_{P_{ij}\in S_i}\mathrm{Tr}[P_{ij}\rho]P_{ij}, \tag{10}$$

where $S_i = \{P_{ij}\}_{j=1}^{2^m-1}$ for each i. As shown by Harada et al. (2024), the following decomposition can be derived from (10), where each unitary U_i is implementable by a Clifford circuit.

$$\mathcal{I}^{\otimes m}(\rho) = (2^{m+1}-1)\Bigg(\sum_{i=1}^{2^m}\frac{1}{2^{m+1}-1}\sum_{j\in\{0,1\}^m}\mathrm{Tr}\left[U_i\left|j\right\rangle\left\langle j\right|U_i^\dagger\rho\right]U_i\left|j\right\rangle\left\langle j\right|U_i^\dagger - \frac{2^m-1}{2^{m+1}-1}\sum_{j\in\{0,1\}^m}\mathrm{Tr}\left[\left|j\right\rangle\left\langle j\right|\rho\right]\rho_j\Bigg), \tag{11}$$

where

$$\rho_j := \sum_{k\in\{0,1\}^m}\frac{1}{2^m-1}(1-\delta_{j,k})\left|k\right\rangle\left\langle k\right|,$$

the set $\{U_i\}_{i=1}^{2^m} \cup \{I^{\otimes m}\}$ consists of operators transforming the computational basis into $2^m + 1$ mutually unbiased bases, and $\delta_{j,k}$ denotes the Kronecker delta.

3.6 Quantum State Teleportation

Key variants of quantum teleportation include state teleportation (Bennett et al., 1993; Bouwmeester et al., 1997; Van Meter et al., 2006), entanglement swapping (Zukowski et al., 1993; Pan et al., 1998), and gate teleportation (Eisert et al., 2000; Huang et al., 2004; Meter III, 2006; Jiang et al., 2007), which respectively allow one-way transfer of quantum states, bi-directional entanglement distribution, and the remote execution of quantum gates (Barral et al., 2024). As a fundamental protocol in quantum communication, quantum state teleportation permits the transmission of an unknown quantum state through the use of a single entangled qubit pair (e-bit) and classical communication channels (Bennett et al., 1993; Bouwmeester et al., 1997; Van Meter et al., 2006; Ren et al., 2017; Cuomo et al., 2020; Cacciapuoti et al., 2020). When Alice intends to transmit a quantum state ρ to Bob, the no-cloning theorem (Wootters and Zurek, 1982; Dieks, 1982; Milonni and Hardies, 1982; Barnum et al., 1996) prohibits her from creating and sending a copy of the state. The quantum teleportation protocol allows her to conduct this transmission. A Bell-state measurement (BSM) is carried out by Alice on the qubit representing the state ρ and on one half of the entangled pair shared with Bob. As a result of the measurement, her two qubits are randomly projected onto one of the four

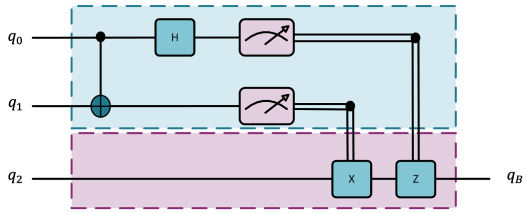

Figure 4: The state teleportation circuit. q_0 is prepared in $|\psi\rangle$ where $\rho = |\psi\rangle\langle\psi|$ is the state Alice intends to transmit. q_1 and q_2 are prepared in the Bell state $|\Phi^+\rangle$. $q_B = |\psi\rangle$ denotes Bob's received qubit.

maximally entangled Bell states (Nielsen and Chuang, 2010), $|\Phi^\pm\rangle$ or $|\Psi^\pm\rangle$, with equal probability. Here,

$$|\Phi^\pm\rangle = \frac{1}{\sqrt{2}}(|00\rangle \pm |11\rangle), |\Psi^\pm\rangle = \frac{1}{\sqrt{2}}(|01\rangle \pm |10\rangle).$$

Bob's entangled qubit collapses into $B^\dagger \rho B$, with $B \in \{I, Z, X, ZX\}$ corresponding to the measurement outcome. Alice subsequently transmits the outcome of her measurement to Bob through two classical bits. Using the received information, Bob performs the appropriate operation on his qubit to reconstruct the original state ρ.

4 Wire Cutting and Adversarial Attacks

Here, we explore how partitioning quantum classifiers by applying wire cutting to their circuits could make them susceptible to adversarial attacks. Wire cutting approaches may be vulnerable to different adversarial manipulations targeting either the measurement or state preparation operations. Adding adversarial perturbations to the prepared states, for example, could allow an attacker to manipulate a quantum classifier's predictions. As we uncover in this section, altering the wire cutting procedure could result in the simulated circuit no longer representing a valid quantum circuit. In this paper, we assume an adversary's goal is to influence the output without causing this issue.

Consider the original wire cutting decomposition in (8). Perturbing one or more of the states within the set $\{\rho_i\}_{i=1}^8$ would lead to the following decomposition, with $\{\tilde{\rho}_i = \tilde{U}_i \rho_i \tilde{U}_i^\dagger\}_{i=1}^8$ and $\{\tilde{U}_i\}_{i=1}^8$ denoting the set of adversarially perturbed states and unitary perturbation operators, respectively.

$$\mathcal{C}_{adv}(\rho) = \sum_{i=1}^{8} c_i \tilde{\rho}_i \mathrm{Tr}(O_i \rho) = \sum_{i=1}^{8} c_i \tilde{U}_i \rho_i \tilde{U}_i^\dagger \mathrm{Tr}(O_i \rho), \quad (12)$$

where $\mathcal{C}_{adv} : \mathcal{L}(\mathcal{H}) \to \mathcal{L}(\mathcal{H})$, with $\mathcal{L}(\mathcal{H})$ denoting the space of square linear operators acting on $\mathcal{H}$. Since unitary operators preserve the trace, it is straightforward to verify $\mathcal{C}_{adv}$ is trace-preserving. Nevertheless, it is not necessarily completely positive[2] and therefore may not constitute a valid quantum channel. In the special case where a similar perturbation operator is applied to all the ρ_is, however, $\mathcal{C}_{adv}$ is a unitary channel:

$$\begin{aligned}\mathcal{C}_{adv}(\rho) &= \sum_{i=1}^{8} c_i \tilde{U} \rho_i \tilde{U}^\dagger \mathrm{Tr}(O_i \rho) \\ &= \tilde{U}\left(\sum_{i=1}^{8} c_i \rho_i \mathrm{Tr}(O_i \rho)\right)\tilde{U}^\dagger \\ &= \tilde{U}(\mathcal{I}(\rho))\tilde{U}^\dagger = \tilde{U}\rho\tilde{U}^\dagger. \end{aligned} \quad (13)$$

In wire cutting, the goal is to simulate a larger quantum circuit by partitioning it into smaller subcircuits. The outcomes of these smaller subcircuits are then combined using classical postprocessing. However, if the wire cutting process is adversarially attacked and the subcircuits are fed with perturbed states, the simulated circuit would differ from the intended one, with $\mathcal{C}_{adv}$ replacing an identity channel in the simulated circuit. Fig. 5 demonstrates a scenario where $\mathcal{C}_{adv}(.) = \tilde{U}(.)\tilde{U}^\dagger$ is a unitary channel, highlighting a connection between adversarially manipulating the state preparation operations in wire cutting and the adversaries in Section 3.4 that are capable of inserting adversarial gates within intermediate layers of a quantum classifier's circuit.

Similar to (12), decomposition (9) could be adversarially manipulated.

$$\mathcal{C}'_{adv}(\rho) = \frac{1}{2^m} \sum_{P \in \{I,X,Y,Z\}^{\otimes m}} \mathrm{Tr}[P(\rho)] \tilde{U}_P P \tilde{U}_P^\dagger, \quad (14)$$

where $\mathcal{C}'_{adv} : \mathcal{L}(\mathcal{H}^{\otimes m}) \to \mathcal{L}(\mathcal{H}^{\otimes m})$ and $\tilde{U}_P \in U(2^m)$ denote unitary perturbation operators. Note that, in general, if we decompose each Pauli string P in (14) using its eigenbasis to feed the eigenstates of P into the subsequent subcircuits, each eigenstate could be adversarially manipulated using a separate unitary operator. Apart from (9), other wire cutting decompositions based on measurement and state preparation operations may be susceptible to similar adversarial attacks. For instance, by adding adversarial perturbations to (11), we

[2] To determine whether $\mathcal{C}_{adv}$ is completely positive (CP), we consider its Choi representation (Choi, 1975). The corresponding Choi matrix is given by $\mathcal{J}(\mathcal{C}_{adv}) = r.(\mathcal{I} \otimes \mathcal{C}_{adv})(|\Phi^+\rangle\langle\Phi^+|)$, where $|\Phi^+\rangle = \frac{1}{\sqrt{r}}\sum_{i=0}^{r-1}|i\rangle \otimes |i\rangle$ is the maximally entangled state, and the dimension of the Hilbert space on which $\mathcal{C}_{adv}$ acts is $r = 2$. $\mathcal{C}_{adv}$ is completely positive if and only if $\mathcal{J}(\mathcal{C}_{adv})$ is positive semidefinite. Any one-qubit density matrix can be expanded in the normalized Pauli matrices, which form an orthonormal basis for the space of 2×2 Hermitian matrices: $\rho = \mathcal{I}(\rho) = (1/2)\sum_{P\in\{I,X,Y,Z\}} \mathrm{Tr}(P\rho)P$. Expanding, in this equation, each Pauli matrix outside the trace in its eigenbasis yields an equation of the form (8) (Peng et al., 2020). An example of a map of the form (12) that is not CP can be obtained by expanding each Pauli matrix outside the trace in its eigenbasis in the following equation: $\mathcal{C}_{adv}(\rho) = (1/2)(\sum_{P\in\{I,Y,Z\}} \mathrm{Tr}(P\rho)P + \mathrm{Tr}(X\rho)\tilde{U}X\tilde{U}^\dagger)$, where $\tilde{U} = Z$. It is straightforward to check that the Choi representation of this map is not positive semidefinite.

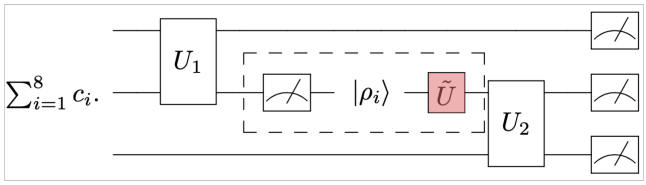

(a) The quantum circuit in Fig. 3.(a) partitioned using the decomposition in (13).

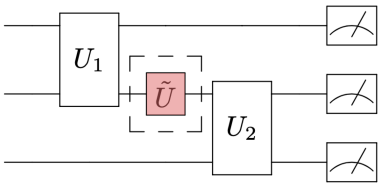

(b) The simulated quantum circuit.

Figure 5: Using the decomposition in (13) rather than (8) to implement wire cutting would result in a simulated quantum circuit with an additional adversarial gate $\tilde{U}$ compared to the original circuit in Fig. 3.(a).

obtain

$$C''_{adv}(\rho) = (2^{m+1}-1)\Bigg(\sum_{i=1}^{2^m} \frac{1}{2^{m+1}-1} \sum_{j\in\{0,1\}^m} \mathrm{Tr}\left[U_i \left|j\right\rangle \left\langle j\right| U_i^\dagger \rho\right] \tilde{U}_{ij} U_i \left|j\right\rangle \left\langle j\right| U_i^\dagger \tilde{U}_{ij}^\dagger - \frac{2^m-1}{2^{m+1}-1} \sum_{j\in\{0,1\}^m} \mathrm{Tr}\left[\left|j\right\rangle \left\langle j\right| \rho\right] \tilde{V}_j \rho_j \tilde{V}_j^\dagger\Bigg), \quad (15)$$

where $\mathcal{C}''_{adv} : \mathcal{L}(\mathcal{H}^{\otimes m}) \to \mathcal{L}(\mathcal{H}^{\otimes m})$ and for all i and j, $\tilde{U}_{ij}$ and $\tilde{V}_j \in U(2^m)$ denote adversarial perturbation operators. In Equations (14) and (15), if a similar perturbation operator is applied to all the prepared states, meaning

$$\tilde{U}_P = \tilde{U}' \quad \forall P \text{ in } (14)$$
$$\tilde{U}_{ij} = \tilde{V}_j = \tilde{U}'' \quad \forall i, j \text{ in } (15),$$

where $\tilde{U}', \tilde{U}'' \in U(2^m)$, $C'_{adv}(.) = \tilde{U}'(.)\tilde{U}'^\dagger$ and $C''_{adv}(.) = \tilde{U}''(.)\tilde{U}''^\dagger$ would represent unitary channels corresponding to $\tilde{U}'$ and $\tilde{U}''$, respectively. Similar to the single-qubit case, when the adversarial channels are unitary, we could interpret the attack as equivalent to inserting an m-qubit adversarial gate acting within the intermediate layers of the simulated circuit.

We assume the adversary's objective is to alter the wire cutting procedure in a way that the adversarial channels implemented are CPTP maps, ensuring the simulated circuit remains a valid quantum circuit, albeit with a manipulated output. In the wire cutting approaches discussed, one straightforward method is to use an identical unitary perturbation operator for manipulating all the prepared states. In the context of attacking quantum classifiers, this approach enables an adversary to learn only a single adversarial unitary operator. With the connection between adversarial attacks targeting the wire cutting procedure in partitioned quantum classifiers and embedding adversarial gates within intermediate layers of a classifier established, we now show a connection between the attack model in Section 3.4 and quantum classifiers partitioned via state teleporation.

5 State Teleportation and Adversarial Attacks

If quantum communication is available, variational quantum algorithms can be partitioned using teleportation-based methods (DiAdamo et al., 2021; Situ et al., 2024), which—unlike circuit cutting—do not introduce exponential sampling overheads and instead consume entangled qubit pairs shared between parties. As with wire cutting, partitioning quantum classifiers via state teleportation can expose them to various adversarial attacks,including scenarios where the sub-circuits are executed in a distributed manner across multiple nodes, with at least one node being malicious. As illustrated in Figure 6, if a malicious node is responsible for executing a sub-circuit and teleporting its output to another node, it may introduce carefully crafted adversarial perturbations into its output before teleporting it. Conversely, a malicious node on the receiving end can adversarially modify the received input state before passing it to the sub-circuit it executes. These scenarios resemble those explored in classical split learning, where adversarial nodes add perturbations to intermediate outputs of the split model (Fan et al., 2023; He et al., 2024). As shown in Figure 6, such adversarial manipulations to the outputs or inputs of the sub-circuits could be thought of as inserting adversarial gates within intermediate layers of the original circuit. Having established the connection between the attack model in Section 3.4 and both wire cutting and state teleporation, we shift our focus in the next section to studying adversarial attacks that implement perturbation gates within intermediate layers of a classifier.

6 Adversarial Perturbation Operators within Intermediate Layers

In this section, we present theorems bounding the predictive confidence shift, $|y_k(\sigma) - \hat{y}_k(\sigma)|$, caused by implementing multiple adversarial gates within intermediate layers of a quantum classifier. A small value of $|y_k(\sigma) - \hat{y}_k(\sigma)|$ indicates robustness and stability against small, malicious changes in the classifier's architecture, as it reflects the model's consistent confidence in label k, whereas a large value suggests sensitivity and significant disruption to the prediction. Especially, in well-trained classifiers, where decision boundaries

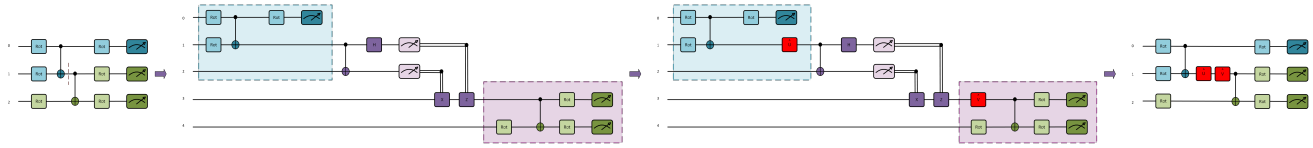

Figure 6: The same circuit from Figure 1, partitioned using state teleportation. This figure illustrates a scenario in which the sub-circuits are executed in a distributed manner across different nodes. If one or both of these nodes are malicious, they could subtly and adversarially influence the circuit's execution. One way to do this is by executing their assigned sub-circuits correctly, but introducing small, carefully crafted perturbations to the output or input of their sub-circuits via perturbation gates $\hat{U}$ or $\hat{V}$. Such an attack is equivalent to implementing $\hat{U}$, $\hat{V}$, or both within intermediate layers of the original circuit.

are far from data points, bounding this quantity indirectly ensures decision boundary stability. Conversely, a large value could indicate that the output has crossed a decision boundary, leading to misclassification.

Our first theorem establishes an upper bound for the predictive confidence shift in any quantum classifier in terms of the sum of the diamond distances between each unitary perturbation channel in (6) and the identity channel. This bound can then be further upper-bounded based on the operator norm. This shows that if all the unitary perturbation operators are close to the identity operator, then the adversarial attack does not trigger a large swing in the classification confidence. The proof is deferred to Appendix A.

Theorem 6.1. *Consider a quantum classifier attacked by inserting adversarial gates within the intermediate layers of its circuit, where the classifier assigns label k to the input state σ with probabilities (1) and (4) before and after the attack, respectively. Then*

$$\begin{aligned}
&|y_k(\sigma) - \hat{y}_k(\sigma)| \\
\leq &\frac{1}{2}\left(\|\mathcal{I}^{\otimes d} - \hat{\mathcal{U}}_0\|_\diamond + \sum_{i=1}^{n} \|\mathcal{I}^{\otimes d_+} - \hat{\mathcal{U}}_i\|_\diamond\right) \\
\leq &\min_{\phi_0 \in U(1)} \|I^{\otimes d} - \phi_0 \hat{U}_0\|_{op} \\
&+ \sum_{i=1}^{n} \min_{\phi_i \in U(1)} \|I^{\otimes d_+} - \phi_i \hat{U}_i\|_{op},
\end{aligned}$$

where $I^{\otimes d}$ and $I^{\otimes d_+}$ represent the $d-$qubit and d_+-qubit identity operators, respectively, with $\mathcal{I}^{\otimes d}$ and $\mathcal{I}^{\otimes d_+}$ denoting their associated identity channels.

Since the operator norm can be upper-bounded by the Hilbert-Schmidt norm, we immediately obtain the following corollary. The Hilbert-Schmidt norm provides a bridge between Theorem 6.1 and Theorem 6.3, presented after the corollary.

Corollary 6.2. *Under the same setup as Theorem 6.1,*

$$\begin{aligned}
|y_k(\sigma) - \hat{y}_k(\sigma)| \leq &\min_{\phi_0 \in U(1)} \|I^{\otimes d} - \phi_0 \hat{U}_0\|_2 \\
&+ \sum_{i=1}^{n} \min_{\phi_i \in U(1)} \|I^{\otimes d_+} - \phi_i \hat{U}_i\|_2.
\end{aligned}$$

In the special case where the adversary perturbs the input state only (i.e., $\hat{U}_i = I^{\otimes d_+}$ for $i \geq 1$), Theorem 6.1 and Corollary 6.2 can be compared to the analysis in Appendix A of (Liao et al., 2021)[3], which bounds the predictive confidence difference in terms of the distance between the density matrices of the original and the adversarially perturbed input states. Our bounds based on the perturbation operators, as opposed to those based on the density operators, allow us to provide a theorem for our more general attack model, outlined in Section 3.4.

The bound in Theorem 6.1 weakens as the attack's strength increases and the distances between the perturbation operators and the identity operator grows. The following theorem provides a probabilistic bound on the predictive confidence shift, even when the perturbation operators are not close to the identity operator. Theorem 6.3 is inspired by Theorem 2 in (Dowling et al., 2024). However, in comparison, besides our expanded attack model, our analysis incorporates a more general model for the quantum classifier. Dowling et al. (2024) focus on binary classification, where the classifier's prediction is determined by the sign of $y(x) = \mathrm{Tr}(ZU\,|\psi(x)\rangle\langle\psi(x)|\,U^\dagger)$, where x is a classical input, with $|\psi(x)\rangle$ representing its encoded quantum state. Here, Z and U denote the Pauli-Z operator acting on a subset of the qubits and a trainable variational unitary, respectively. Compared to this setting, as outlined in Section 3.2, we consider K-multiclass classification, a general POVM Π_k, and a CPTP map $\mathcal{E}$ which encompasses the specific case of the unitary evolution described by $U(.)U^\dagger$. Due to our more general setting, the out-of-time-ordered correlator (OTOC) (Larkin and Ovchinnikov, 1969; Sekino and Susskind, 2008; Shenker and Stanford, 2014; Maldacena et al., 2016) does not appear in our final bound in the same way it does in Dowling et al.'s analysis (2024). Instead, our analysis, which can be

[3] For additional related theorems, see Theorem 1 in (Dowling et al., 2024) and Lemma 2 in (Anil et al., 2024).

found in Appendix B, provides a bound based on the Hilbert-Schmidt distance between $\mathcal{E}(\Pi_k)^\dagger$ and $\hat{\mathcal{E}}(\Pi_k)^\dagger$, where $\mathcal{E}^\dagger$ and $\hat{\mathcal{E}}^\dagger$ denote the adjoins of the CPTP maps $\mathcal{E}$ and $\hat{\mathcal{E}}$ described in (1) and (6), respectively. This can be further bounded in terms of the Hilbert-Schmidt distances between the unitary perturbation operators and the identity operator.

Unlike Theorem 6.1, we simplify our analysis for the following theorem by excluding the presence of ancilla bits from the classifier's input and assuming the circuit's induced CPTP map $\mathcal{E}$ is unital. Furthermore, similar to Dowling et al. (2024), we assume the classifier's input σ is selected Haar-randomly. Note that, this is more of a simplifying assumption rather than a realistic one (Liao et al., 2021), and may lead to pessimistic results concerning the adversarial vulnerability of quantum classifiers (e.g., see (Liu and Wittek, 2020)). Nevertheless, it provides useful tools for theoretical analysis, which could pave the way for future work that relaxes this assumption.

Theorem 6.3 establishes a probabilistic bound for $|y_k(\sigma) - \hat{y}_k(\sigma)|$ by employing Chebyshev's inequality. Appendix B presents the proof of this theorem.

Theorem 6.3. *If $\sigma = W|0\rangle\langle 0|W^\dagger \in \mathcal{D}(\mathcal{H}^{\otimes d})$, with W denoting a unitary operator sampled from the Haar ensemble[4], then for any $\delta > 0$, $|y_k(\sigma) - \hat{y}_k(\sigma)| < \delta$ holds with probability at least*

$$1 - \frac{4\|\Pi_k\|_2^2 \left(\sum_{i=0}^{n} \|I^{\otimes d} - \hat{U}_i\|_2\right)^2}{D(D+1)\delta^2},$$

where $D := 2^d$, $y_k(\sigma) = \mathrm{Tr}(\Pi_k \mathcal{E}(\sigma)), \hat{y}_k(\sigma) = \mathrm{Tr}(\Pi_k \hat{\mathcal{E}}(\hat{U}_0 \sigma \hat{U}_0^\dagger))$, and each $\hat{U}_i$ denotes a unitary perturbation operator in (5).

7 Experimental Results

This section focuses on experimentally examining the impact of planting perturbation operators within layers of a simulated quantum classifier. We evaluate how inserting one or multiple global or local adversarial gates at different circuit depths influences the performance of the model. We also experimentally evaluate the bound in Theorem 6.3 and assess its tightness.

Using Pennylane (Bergholm et al., 2018) and Keras (Chollet et al., 2015), we simulate quantum classifiers in a noiseless setting for binary and four-class classification on the MNIST (LeCun et al., 2010) and FMNIST (Xiao et al., 2017) datasets, both downsampled to 16×16 pixels. We further include CIFAR-10 (Krizhevsky et al., 2009), evaluated only for binary classification. We employ quantum classifiers based on hardware-efficient ansätze (Kandala et al., 2017), consisting of ℓ layers, where each layer contains a rotation unit followed by an entangling unit. The adversarial unitaries we implement within their intermediate layers follow the same structure: each perturbation operator consists of multiple layers of gates, and each layer comprises one rotation block and one entangling block. The full architecture of our classifiers is provided in Appendix C.1, and their pre-attack performance is reported in Appendix C.2.

We study the effects of implementing one or multiple adversarial gates within the intermediate layers of our classifiers and investigate two settings for these adversarial gates: global gates that can affect all the qubits, and local gates that can only impact a subset of qubits. We assess the effectiveness of each adversarial scenario by measuring the misclassification rate it induces at a given attack strength, where the attack strength is defined as the sum of the distances between the adversarial perturbation operators and the identity operator. For each scenario, we record the misclassification rate and the corresponding attack strength at every training epoch, and then plot misclassification rate versus attack strength to analyze how their relationship evolves over time. Appendix C.3.1 details the implemented attack scenarios, the training procedure for the adversarial layers, their hyperparameters, and our evaluation methodology.

Our experiments indicate that partitioned classifiers could be more vulnerable to adversarial attacks than unpartitioned ones in two ways. First, unlike unpartitioned classifiers which can only be attacked by manipulating thier input states, partitioned ones can by manipulated by adding adversarial gates within their layers, and we observe that in some cases implementing adversarial gates within intermediate layers of quantum classifiers can produce more potent adversarial effects than manipulating their input states. Second, partitioned classifiers expose multiple attack surfaces, as adversaries can deploy several adversarial gates within their layers. Appendix C.3.2 analyzes our experimental results in greater detail, while detailed figures corresponding to our experiments are presented in Appendices C.3.3 and C.3.4.

The bound provided by Theorem 6.3 is particularly useful when the pre-attack probabilities assigned by the classifier to each label are known. Using this bound, especially in the binary classification setting, we can predict whether an adversarial attack is likely to flip the classifier's predicted label. We experimentally investigate the tightness of the bound provided by this theorem and its practical usefulness. Our experiments, detailed in Appendix C.4, show that the theoretical bound on $|y_k(\sigma) - \hat{y}_k(\sigma)|$ often provides useful bounds on the values of $\hat{y}_k(\sigma)$ during training the adversarial gates in practice, particularly when the attack strength is small. Since increasing the attack strength generally results in less stealthy attacks, these results demonstrate the practical utility of our bound in scenarios where adversaries implement stealthy attacks. Recall that $\hat{y}_k(\sigma)$ and $y_k(\sigma)$ denote the probabilities of assigning label k to an input sample σ before and after an adversarial attack, respectively.

[4] It suffices for our proof that W is drawn from a unitary 2-design (Dankert et al., 2009).

8 Conclusions

In this work, we shed light on the adversarial robustness of quantum classifiers when partitioned using wire cutting or state teleportation and demonstrated a connection between attacks targeting partitioned classifiers and implementing adversarial gates within intermediate layers of quantum classifiers. We bound the shift in quantum classifiers' confidence resulting from inserting multiple adversarial gates within their architecture and empirically studied the effects of planting these gates at different circuit depths. Our findings contribute to a deeper understanding of quantum classifiers' adversarial robustness, paving the way for further exploration into their resilience to attacks targeting various quantum circuit distribution methods.

Acknowledgements

This research has been funded by the research project "Quantum Software Consortium: Exploring Distributed Quantum Solutions for Canada" (QSC). QSC is financed under the National Sciences and Engineering Research Council of Canada (NSERC) Alliance Consortia Quantum Grants #ALLRP587590-23.

References

Amira Abbas, David Sutter, Christa Zoufal, Aurélien Lucchi, Alessio Figalli, and Stefan Woerner. The power of quantum neural networks. *Nature Computational Science*, 1(6):403–409, 2021.

Rudolf Ahlswede, Igor Bjelaković, Holger Boche, and Janis Nötzel. Quantum capacity under adversarial quantum noise: Arbitrarily varying quantum channels. *Communications in Mathematical Physics*, 317(1):103–156, 2013.

Gautham Anil, Vishnu Vinod, and Apurva Narayan. Generating universal adversarial perturbations for quantum classifiers. In *Proceedings of the 38th AAAI Conference on Artificial Intelligence*, volume 38, pages 10891–10899, 2024.

Yijie Bai, Yanjiao Chen, Hanlei Zhang, Wenyuan Xu, Haiqin Weng, and Dou Goodman. {VILLAIN}: Backdoor attacks against vertical split learning. In *Proceedings of the 32nd USENIX Security Symposium*, pages 2743–2760, 2023.

Soumen Bajpayee, Sarbani Sen, Anipriyo Mandal, and Imon Mukherjee. Quantum teleportation under siege: Analyzing noise attack with virtual entanglement. In *Proceedings of the 2024 IEEE Calcutta Conference (CALCON)*, pages 1–5, 2024.

Jonathan M Baker, Casey Duckering, Alexander Hoover, and Frederic T Chong. Time-sliced quantum circuit partitioning for modular architectures. In *Proceedings of the 17th ACM International Conference on Computing Frontiers*, pages 98–107, 2020.

Howard Barnum, Carlton M Caves, Christopher A Fuchs, Richard Jozsa, and Benjamin Schumacher. Noncommuting mixed states cannot be broadcast. *Physical Review Letters*, 76(15):2818, 1996.

David Barral, F Javier Cardama, Guillermo Díaz, Daniel Faílde, Iago F Llovo, Mariamo Mussa Juane, Jorge Vázquez-Pérez, Juan Villasuso, César Piñeiro, Natalia Costas, et al. Review of distributed quantum computing. from single qpu to high performance quantum computing. *arXiv preprint arXiv:2404.01265*, 2024.

Charles H Bennett, Gilles Brassard, Claude Crépeau, Richard Jozsa, Asher Peres, and William K Wootters. Teleporting an unknown quantum state via dual classical and einstein-podolsky-rosen channels. *Physical review letters*, 70(13): 1895, 1993.

Ville Bergholm, Josh Izaac, Maria Schuld, Christian Gogolin, Shahnawaz Ahmed, Vishnu Ajith, M Sohaib Alam, Guillermo Alonso-Linaje, B AkashNarayanan, Ali Asadi, et al. Pennylane: Automatic differentiation of hybrid quantum-classical computations. *arXiv preprint arXiv:1811.04968*, 2018.

Pablo Bermejo, Paolo Braccia, Manuel S Rudolph, Zoë Holmes, Lukasz Cincio, and M Cerezo. Quantum convolutional neural networks are (effectively) classically simulable. *arXiv preprint arXiv:2408.12739*, 2024.

Kishor Bharti, Alba Cervera-Lierta, Thi Ha Kyaw, Tobias Haug, Sumner Alperin-Lea, Abhinav Anand, Matthias Degroote, Hermanni Heimonen, Jakob S Kottmann, Tim Menke, et al. Noisy intermediate-scale quantum algorithms. *Reviews of Modern Physics*, 94(1):015004, 2022.

Debasmita Bhoumik, Ritajit Majumdar, Amit Saha, and Susmita Sur-Kolay. Distributed scheduling of quantum circuits with noise and time optimization. *arXiv preprint arXiv:2309.06005*, 2023.

Jacob Biamonte, Peter Wittek, Nicola Pancotti, Patrick Rebentrost, Nathan Wiebe, and Seth Lloyd. Quantum machine learning. *Nature*, 549(7671):195–202, 2017.

Danilo Boschi, Salvatore Branca, Francesco De Martini, Lucien Hardy, and Sandu Popescu. Experimental realization of teleporting an unknown pure quantum state via dual classical and einstein-podolsky-rosen channels. *Physical Review Letters*, 80(6):1121, 1998.

Dik Bouwmeester, Jian-Wei Pan, Klaus Mattle, Manfred Eibl, Harald Weinfurter, and Anton Zeilinger. Experimental quantum teleportation. *Nature*, 390(6660):575–579, 1997.

Sebastian Brandhofer, Ilia Polian, and Kevin Krsulich. Optimal partitioning of quantum circuits using gate cuts and wire cuts. *IEEE Transactions on Quantum Engineering*, 2023.

Sergey Bravyi, Graeme Smith, and John A Smolin. Trading classical and quantum computational resources. *Physical Review X*, 6(2):021043, 2016.

Lukas Brenner, Christophe Piveteau, and David Sutter. Optimal wire cutting with classical communication. *arXiv preprint arXiv:2302.03366*, 2023.

Angela Sara Cacciapuoti, Marcello Caleffi, Rodney Van Meter, and Lajos Hanzo. When entanglement meets classical communications: Quantum teleportation for the quantum internet. *IEEE Transactions on Communications*, 68(6): 3808–3833, 2020.

Nadir Casciola, Edoardo Giusto, Emanuele Dri, Daniel Oliveira, Paolo Rech, and Bartolomeo Montrucchio. Understanding the impact of cutting in quantum circuits reliability to transient faults. In *Proceedings of the 28th IEEE International Symposium on On-Line Testing and Robust System Design (IOLTS)*, pages 1–7, 2022.

Marco Cerezo, Andrew Arrasmith, Ryan Babbush, Simon C Benjamin, Suguru Endo, Keisuke Fujii, Jarrod R McClean, Kosuke Mitarai, Xiao Yuan, Lukasz Cincio, et al. Variational quantum algorithms. *Nature Reviews Physics*, 3(9): 625–644, 2021.

Marco Cerezo, Guillaume Verdon, Hsin-Yuan Huang, Lukasz Cincio, and Patrick J Coles. Challenges and opportunities in quantum machine learning. *Nature Computational Science*, 2(9):567–576, 2022.

Marco Cerezo, Martin Larocca, Diego García-Martín, Nelson L Diaz, Paolo Braccia, Enrico Fontana, Manuel S Rudolph, Pablo Bermejo, Aroosa Ijaz, Supanut Thanasilp, et al. Does provable absence of barren plateaus imply classical simulability? or, why we need to rethink variational quantum computing. *arXiv preprint arXiv:2312.09121*, 2023.

Mahdi Chehimi and Walid Saad. Quantum federated learning with quantum data. In *Proceedings of the 47th IEEE International Conference on Acoustics, Speech and Signal Processing (ICASSP)*, pages 8617–8621, 2022.

Daniel Chen, Betis Baheri, Vipin Chaudhary, Qiang Guan, Ning Xie, and Shuai Xu. Approximate quantum circuit reconstruction. In *Proceedings of the 3rd IEEE International Conference on Quantum Computing and Engineering (QCE)*, pages 509–515, 2022.

Daniel T Chen, Ethan H Hansen, Xinpeng Li, Vinooth Kulkarni, Vipin Chaudhary, Bin Ren, Qiang Guan, Sanmukh Kuppannagari, Ji Liu, and Shuai Xu. Efficient quantum circuit cutting by neglecting basis elements. In *Proceedings of the 37th IEEE International Parallel and Distributed Processing Symposium Workshops (IPDPSW)*, pages 517–523, 2023a.

Daniel T Chen, Ethan H Hansen, Xinpeng Li, Aaron Orenstein, Vinooth Kulkarni, Vipin Chaudhary, Qiang Guan, Ji Liu, Yang Zhang, and Shuai Xu. Online detection of golden circuit cutting points. In *Proceedings of the 4th IEEE International Conference on Quantum Computing and Engineering (QCE)*, volume 1, pages 26–31, 2023b.

Liangjun Chen, Lili Yan, and Shibin Zhang. Robust quantum federated learning with noise. *Physica Scripta*, 99(7): 076003, 2024.

Man-Duen Choi. Completely positive linear maps on complex matrices. *Linear algebra and its applications*, 10(3):285–290, 1975.

François Chollet et al. Keras. https://keras.io, 2015.

Cheng Chu, Lei Jiang, and Fan Chen. Cryptoqfl: quantum federated learning on encrypted data. In *Proceedings of the 2023 IEEE International Conference on Quantum Computing and Engineering (QCE)*, volume 1, pages 1231–1237, 2023.

Jeremy Cohen, Elan Rosenfeld, and Zico Kolter. Certified adversarial robustness via randomized smoothing. In *Proceedings of the 36th International Conference on Machine Learning (ICML)*, pages 1310–1320, 2019.

Iris Cong, Soonwon Choi, and Mikhail D Lukin. Quantum convolutional neural networks. *Nature Physics*, 15(12): 1273–1278, 2019.

Daniele Cuomo, Marcello Caleffi, and Angela Sara Cacciapuoti. Towards a distributed quantum computing ecosystem. *IET Quantum Communication*, 1(1):3–8, 2020.

Daniele Cuomo, Marcello Caleffi, Kevin Krsulich, Filippo Tramonto, Gabriele Agliardi, Enrico Prati, and Angela Sara Cacciapuoti. Optimized compiler for distributed quantum computing. *ACM Transactions on Quantum Computing*, 4 (2):1–29, 2023.

Christoph Dankert, Richard Cleve, Joseph Emerson, and Etera Livine. Exact and approximate unitary 2-designs and their application to fidelity estimation. *Physical Review A*, 80(1):012304, 2009.

Stephen DiAdamo, Marco Ghibaudi, and James Cruise. Distributed quantum computing and network control for accelerated vqe. *IEEE Transactions on Quantum Engineering*, 2:1–21, 2021.

DGBJ Dieks. Communication by epr devices. *Physics Letters A*, 92(6):271–272, 1982.

Neil Dowling, Maxwell T West, Angus Southwell, Azar C Nakhl, Martin Sevior, Muhammad Usman, and Kavan Modi. Adversarial robustness guarantees for quantum classifiers. *arXiv preprint arXiv:2405.10360*, 2024.

Yuxuan Du, Min-Hsiu Hsieh, Tongliang Liu, Dacheng Tao, and Nana Liu. Quantum noise protects quantum classifiers against adversaries. *Physical Review Research*, 3(2): 023153, 2021.

Cynthia Dwork, Frank McSherry, Kobbi Nissim, and Adam Smith. Calibrating noise to sensitivity in private data analysis. In *Proceedings of the 3rd Conference on Theory of Cryptography (TCC)*, pages 265–284, 2006.

Andrew Eddins, Mario Motta, Tanvi P Gujarati, Sergey Bravyi, Antonio Mezzacapo, Charles Hadfield, and Sarah Sheldon. Doubling the size of quantum simulators by entanglement forging. *PRX Quantum*, 3(1):010309, 2022.

Jens Eisert, Kurt Jacobs, Polykarpos Papadopoulos, and Martin B Plenio. Optimal local implementation of nonlocal quantum gates. *Physical Review A*, 62(5):052317, 2000.

Suguru Endo, Simon C Benjamin, and Ying Li. Practical quantum error mitigation for near-future applications. *Physical Review X*, 8(3):031027, 2018.

Ege Erdoğan, Alptekin Küpçü, and A Ercüment Çiçek. Unsplit: Data-oblivious model inversion, model stealing, and label inference attacks against split learning. In *Proceedings of the 21st Workshop on Privacy in the Electronic Society*, pages 115–124, 2022.

Mingyuan Fan, Cen Chen, Chengyu Wang, Wenmeng Zhou, and Jun Huang. On the robustness of split learning against adversarial attacks. In *Proceedings of the 26th European Conference on Artificial Intelligence (ECAI)*, pages 668–675, 2023.

Davide Ferrari, Angela Sara Cacciapuoti, Michele Amoretti, and Marcello Caleffi. Compiler design for distributed quantum computing. *IEEE Transactions on Quantum Engineering*, 2:1–20, 2021.

Davide Ferrari, Stefano Carretta, and Michele Amoretti. A modular quantum compilation framework for distributed quantum computing. *IEEE Transactions on Quantum Engineering*, 4:1–13, 2023.

Chong Fu, Xuhong Zhang, Shouling Ji, Jinyin Chen, Jingzheng Wu, Shanqing Guo, Jun Zhou, Alex X Liu, and Ting Wang. Label inference attacks against vertical federated learning. In *Proceedings of the 31st USENIX Security Symposium*, pages 1397–1414, 2022.

Keisuke Fujii, Kaoru Mizuta, Hiroshi Ueda, Kosuke Mitarai, Wataru Mizukami, and Yuya O Nakagawa. Deep variational quantum eigensolver: a divide-and-conquer method for solving a larger problem with smaller size quantum computers. *PRX Quantum*, 3(1):010346, 2022.

Ranjani G Sundaram, Himanshu Gupta, and CR Ramakrishnan. Efficient distribution of quantum circuits. In *Proceedings of the 35th International Symposium on Distributed Computing (DISC)*, pages 41–1, 2021.

Saurabh Gajbhiye, Priyanka Singh, and Shaifu Gupta. Data poisoning attack by label flipping on splitfed learning. In *Proceedings of the 5th International Conference on Recent Trends in Image Processing and Pattern Recognition (RTIP2R)*, pages 391–405, 2022.

Sayan Gangopadhyay, Tiejun Wang, Atefeh Mashatan, and Shohini Ghose. Controlled quantum teleportation in the presence of an adversary. *Physical Review A*, 106(5): 052433, 2022.

Yansong Gao, Minki Kim, Sharif Abuadbba, Yeonjae Kim, Chandra Thapa, Kyuyeon Kim, Seyit A Camtepe, Hyoungshick Kim, and Surya Nepal. End-to-end evaluation of federated learning and split learning for internet of things. *arXiv preprint arXiv:2003.13376*, 2020.

Grzegorz Gawron and Philip Stubbings. Feature space hijacking attacks against differentially private split learning. *arXiv preprint arXiv:2201.04018*, 2022.

Gian Gentinetta, Friederike Metz, and Giuseppe Carleo. Overhead-constrained circuit knitting for variational quantum dynamics. *Quantum*, 8:1296, 2024.

Pranav Gokhale, Olivia Angiuli, Yongshan Ding, Kaiwen Gui, Teague Tomesh, Martin Suchara, Margaret Martonosi, and Frederic T Chong. $o(n^3)$ measurement cost for variational quantum eigensolver on molecular hamiltonians. *IEEE Transactions on Quantum Engineering*, 1:1–24, 2020.

Weiyuan Gong and Dong-Ling Deng. Universal adversarial examples and perturbations for quantum classifiers. *National Science Review*, 9(6):nwab130, 2022.

Weiyuan Gong, Dong Yuan, Weikang Li, and Dong-Ling Deng. Enhancing quantum adversarial robustness by randomized encodings. *arXiv preprint arXiv:2212.02531*, 2022.

Diego Guala, Shaoming Zhang, Esther Cruz, Carlos A Riofrío, Johannes Klepsch, and Juan Miguel Arrazola. Practical overview of image classification with tensor-network quantum circuits. *Scientific Reports*, 13(1):4427, 2023.

Ji Guan, Wang Fang, and Mingsheng Ying. Robustness verification of quantum classifiers. In *Proceedings of the 33rd International Conference on Computer Aided Verification (CAV)*, pages 151–174, 2021.

Gian Giacomo Guerreschi and Mikhail Smelyanskiy. Practical optimization for hybrid quantum-classical algorithms. *arXiv preprint arXiv:1701.01450*, 2017.

Otkrist Gupta and Ramesh Raskar. Distributed learning of deep neural network over multiple agents. *Journal of Network and Computer Applications*, 116:1–8, 2018.

Jeongwan Haah, Robin Kothari, Ryan O'Donnell, and Ewin Tang. Query-optimal estimation of unitary channels in diamond distance. In *Proceedings of the 64th IEEE Annual Symposium on Foundations of Computer Science (FOCS)*, pages 363–390, 2023.

Hala Hamdoun and Alaa Sagheer. Information security through controlled quantum teleportation networks. *Digital Communications and Networks*, 6(4):463–470, 2020.

Hiroyuki Harada, Kaito Wada, and Naoki Yamamoto. Doubly optimal parallel wire cutting without ancilla qubits. *PRX Quantum*, 5(4):040308, 2024.

Aram W Harrow and Angus Lowe. Optimal quantum circuit cuts with application to clustered hamiltonian simulation. *arXiv preprint arXiv:2403.01018*, 2024.

Yunxiao He, Chunqiang Hu, Yuwen Pu, Jiahao Chen, and Xingwang Li. Advusl: Targeted adversarial attack against u-shaped split learning. In *Proceedings of the 21st IEEE International Conference on Mobile Ad-Hoc and Smart Systems (MASS)*, pages 357–363, 2024.

Christiaan Heunen and Pablo Andres Martinez. Automated distribution of quantum circuits. *Physical Review A*, 100: 032308, 2019.

Stephen A Holmes. Quantum teleportation: Mitigating entangled qubit capture over insecure networks. In *Proceedings of the 2025 IEEE Conference on Computer Communications Workshops (INFOCOM WKSHPS)*, pages 1–6, 2025.

Mahboobeh Houshmand, Zahra Mohammadi, Mariam Zomorodi-Moghadam, and Monireh Houshmand. An evolutionary approach to optimizing teleportation cost in distributed quantum computation. *International Journal of Theoretical Physics*, 59(4):1315–1329, 2020.

Mark Howard and Earl Campbell. Application of a resource theory for magic states to fault-tolerant quantum computing. *Physical review letters*, 118(9):090501, 2017.

Chenyi Huang and Shibin Zhang. Enhancing adversarial robustness of quantum neural networks by adding noise layers. *New Journal of Physics*, 25(8):083019, 2023.

Hsin-Yuan Huang, Michael Broughton, Jordan Cotler, Sitan Chen, Jerry Li, Masoud Mohseni, Hartmut Neven, Ryan Babbush, Richard Kueng, John Preskill, et al. Quantum advantage in learning from experiments. *Science*, 376 (6598):1182–1186, 2022.

Jhih-Cing Huang, Yu-Lin Tsai, Chao-Han Huck Yang, Cheng-Fang Su, Chia-Mu Yu, Pin-Yu Chen, and Sy-Yen Kuo. Certified robustness of quantum classifiers against adversarial examples through quantum noise. In *Proceedings of the 48th IEEE International Conference on Acoustics, Speech and Signal Processing (ICASSP)*, pages 1–5, 2023.

Yin Huang, Lei Wang, and Jie Xu. Quantum entanglement path selection and qubit allocation via adversarial group neural bandits. *IEEE/ACM Transactions on Networking*, 2024.

Yun-Feng Huang, Xi-Feng Ren, Yong-Sheng Zhang, Lu-Ming Duan, and Guang-Can Guo. Experimental teleportation of a quantum controlled-not gate. *Physical review letters*, 93(24):240501, 2004.

Liang Jiang, Jacob M Taylor, Anders S Sørensen, and Mikhail D Lukin. Distributed quantum computation based on small quantum registers. *Physical Review A*, 76(6): 062323, 2007.

Abhinav Kandala, Antonio Mezzacapo, Kristan Temme, Maika Takita, Markus Brink, Jerry M Chow, and Jay M Gambetta. Hardware-efficient variational quantum eigensolver for small molecules and quantum magnets. *nature*, 549(7671):242–246, 2017.

Amena Khatun and Muhammad Usman. Classical autoencoder distillation of quantum adversarial manipulations. *arXiv preprint arXiv:2504.09216*, 2025a.

Amena Khatun and Muhammad Usman. Quantum transfer learning with adversarial robustness for classification of high-resolution image datasets. *Advanced Quantum Technologies*, 8(1):2400268, 2025b.

Diederik P. Kingma and Jimmy Ba. Adam: A method for stochastic optimization. *arXiv preprint arXiv:1412.6980*, 2017.

Jakub Konečnỳ, H Brendan McMahan, Daniel Ramage, and Peter Richtárik. Federated optimization: Distributed machine learning for on-device intelligence. *arXiv preprint arXiv:1610.02527*, 2016a.

Jakub Konečnỳ, H Brendan McMahan, Felix X Yu, Peter Richtárik, Ananda Theertha Suresh, and Dave Bacon. Federated learning: Strategies for improving communication efficiency. *arXiv preprint arXiv:1610.05492*, 2016b.

Alex Krizhevsky, Geoffrey Hinton, et al. Learning multiple layers of features from tiny images. 2009.

Ajay Kumar and Sunita Garhwal. State-of-the-art survey of quantum cryptography. *Archives of Computational Methods in Engineering*, 28(5):3831–3868, 2021.

Niraj Kumar, Jamie Heredge, Changhao Li, Shaltiel Eloul, Shree Hari Sureshbabu, and Marco Pistoia. Expressive variational quantum circuits provide inherent privacy in federated learning. *arXiv preprint arXiv:2309.13002*, 2023.

Anatoly I Larkin and Yu N Ovchinnikov. Quasiclassical method in the theory of superconductivity. *Sov Phys JETP*, 28(6):1200–1205, 1969.

Martin Larocca, Supanut Thanasilp, Samson Wang, Kunal Sharma, Jacob Biamonte, Patrick J Coles, Lukasz Cincio, Jarrod R McClean, Zoë Holmes, and M Cerezo. A review of barren plateaus in variational quantum computing. *arXiv preprint arXiv:2405.00781*, 2024.

Jay Lawrence, Časlav Brukner, and Anton Zeilinger. Mutually unbiased binary observable sets on n qubits. *Physical Review A*, 65(3):032320, 2002.

Yann LeCun, Corinna Cortes, and Christopher Burges. Mnist handwritten digit database. AT&T Labs, 2010. [Online]. Available: http://yann.lecun.com/exdb/mnist.

Changhao Li, Niraj Kumar, Zhixin Song, Shouvanik Chakrabarti, and Marco Pistoia. Privacy-preserving quantum federated learning via gradient hiding. *Quantum Science and Technology*, 9(3):035028, 2024a.

Weikang Li, Sirui Lu, and Dong-Ling Deng. Quantum federated learning through blind quantum computing. *Science China Physics, Mechanics & Astronomy*, 64(10):100312, 2021.

Xinpeng Li, Vinooth Kulkarni, Daniel T Chen, Qiang Guan, Weiwen Jiang, Ning Xie, Shuai Xu, and Vipin Chaudhary. Efficient circuit wire cutting based on commuting groups. In *Proceedings of the 5th IEEE International Conference on Quantum Computing and Engineering (QCE)*, volume 1, pages 117–123, 2024b.

Haoran Liao, Ian Convy, William J Huggins, and K Birgitta Whaley. Robust in practice: Adversarial attacks on quantum machine learning. *Physical Review A*, 103(4):042427, 2021.

Ji Liu, Alvin Gonzales, and Zain H Saleem. Classical simulators as quantum error mitigators via circuit cutting. *arXiv preprint arXiv:2212.07335*, 2022.

Nana Liu and Peter Wittek. Vulnerability of quantum classification to adversarial perturbations. *Physical Review A*, 101 (6):062331, 2020.

Yunchao Liu, Srinivasan Arunachalam, and Kristan Temme. A rigorous and robust quantum speed-up in supervised machine learning. *Nature Physics*, 17(9):1013–1017, 2021.

Angus Lowe, Matija Medvidović, Anthony Hayes, Lee J O'Riordan, Thomas R Bromley, Juan Miguel Arrazola, and Nathan Killoran. Fast quantum circuit cutting with randomized measurements. *Quantum*, 7:934, 2023.

Sirui Lu, Lu-Ming Duan, and Dong-Ling Deng. Quantum adversarial machine learning. *Physical Review Research*, 2(3):033212, 2020.

Ritajit Majumdar and Christopher J Wood. Error mitigated quantum circuit cutting. *arXiv preprint arXiv:2211.13431*, 2022.

Juan Maldacena, Stephen H Shenker, and Douglas Stanford. A bound on chaos. *Journal of High Energy Physics*, 2016 (8):1–17, 2016.

Yunlong Mao, Zexi Xin, Zhenyu Li, Jue Hong, Qingyou Yang, and Sheng Zhong. Secure split learning against property inference, data reconstruction, and feature space hijacking attacks. In *Proceedings of the 28th European Symposium on Research in Computer Security (ESORICS)*, pages 23–43. Springer, 2023.

Walid El Maouaki, Nouhaila Innan, Alberto Marchisio, Taoufik Said, Mohamed Bennai, and Muhammad Shafique. Qfal: Quantum federated adversarial learning. *arXiv preprint arXiv:2502.21171*, 2025.

Alberto Marchisio, Emman Sychiuco, Muhammad Kashif, and Muhammad Shafique. Cutting is all you need: Execution of large-scale quantum neural networks on limited-qubit devices. *arXiv preprint arXiv:2412.04844*, 2024.

Simon C Marshall, Casper Gyurik, and Vedran Dunjko. High dimensional quantum machine learning with small quantum computers. *Quantum*, 7:1078, 2023.

Brendan McMahan, Eider Moore, Daniel Ramage, Seth Hampson, and Blaise Aguera y Arcas. Communication-efficient learning of deep networks from decentralized data. In *Proceedings of the 20th International Conference on Artificial Intelligence and Statistics (AISTATS 2017)*, pages 1273–1282, 2017.

Rodney Doyle Van Meter III. Architecture of a quantum multicomputer optimized for shor's factoring algorithm. *arXiv preprint quant-ph/0607065*, 2006.

Qiang Miao and Thomas Barthel. Isometric tensor network optimization for extensive hamiltonians is free of barren plateaus. *Physical Review A*, 109(5):L050402, 2024.

Peter W Milonni and ML Hardies. Photons cannot always be replicated. *Physics Letters A*, 92(7), 1982.

Kosuke Mitarai and Keisuke Fujii. Constructing a virtual two-qubit gate by sampling single-qubit operations. *New Journal of Physics*, 23(2):023021, 2021a.

Kosuke Mitarai and Keisuke Fujii. Overhead for simulating a non-local channel with local channels by quasiprobability sampling. *Quantum*, 5:388, 2021b.

Kosuke Mitarai, Makoto Negoro, Masahiro Kitagawa, and Keisuke Fujii. Quantum circuit learning. *Physical Review A*, 98(3):032309, 2018.

Giuseppe Montalbano and Leonardo Banchi. Quantum adversarial learning for kernel methods. *Quantum Machine Intelligence*, 7(1):15, 2025.

Ryo Nagai, Shu Kanno, Yuki Sato, and Naoki Yamamoto. Quantum channel decomposition with preselection and postselection. *Physical Review A*, 108(2):022615, 2023.

Saw Nang Paing, Jason William Setiawan, Shehbaz Tariq, Muhammad Talha Rahim, Kyesan Lee, and Hyundong Shin. Counterfactual anonymous quantum teleportation in the presence of adversarial attacks and channel noise. *Sensors*, 22(19):7587, 2022.

Bhaskara Narottama and Soo Young Shin. Federated quantum neural network with quantum teleportation for resource optimization in future wireless communication. *IEEE Transactions on Vehicular Technology*, 72(11):14717–14733, 2023.

Simon Neves, Laura dos Santos Martins, Verena Yacoub, Pascal Lefebvre, Ivan Šupić, Damian Markham, and Eleni Diamanti. Experimentally certified transmission of a quantum message through an untrusted and lossy quantum channel via bell's theorem. *PRX Quantum*, 6(3):030312, 2025.

Michael A Nielsen and Isaac L Chuang. *Quantum Computation and Quantum Information*. Cambridge University Press, 2010.

Eesa Nikahd, Naser Mohammadzadeh, Mehdi Sedighi, and Morteza Saheb Zamani. Automated window-based partitioning of quantum circuits. *Physica Scripta*, 96(3):035102, 2021.

Jian-Wei Pan, Dik Bouwmeester, Harald Weinfurter, and Anton Zeilinger. Experimental entanglement swapping: entangling photons that never interacted. *Physical Review Letters*, 80(18):3891, 1998.

Georgios Papadopoulos, Shaltiel Eloul, Yash Satsangi, Jamie Heredge, Niraj Kumar, Chun-Fu Chen, and Marco Pistoia. A numerical gradient inversion attack in variational quantum neural-networks. *arXiv preprint arXiv:2504.12806*, 2025.

Hakop Pashayan, Joel J Wallman, and Stephen D Bartlett. Estimating outcome probabilities of quantum circuits using quasiprobabilities. *Physical review letters*, 115(7):070501, 2015.

Dario Pasquini, Giuseppe Ateniese, and Massimo Bernaschi. Unleashing the tiger: Inference attacks on split learning. In *Proceedings of the 27th ACM SIGSAC Conference on Computer and Communications Security (CCS)*, pages 2113–2129, 2021.

Edwin Pednault. An alternative approach to optimal wire cutting without ancilla qubits. *arXiv preprint arXiv:2303.08287*, 2023.

Tianyi Peng, Aram W Harrow, Maris Ozols, and Xiaodi Wu. Simulating large quantum circuits on a small quantum computer. *Physical review letters*, 125(15):150504, 2020.

Adrián Pérez-Salinas, Radoica Draškić, Jordi Tura, and Vedran Dunjko. Shallow quantum circuits for deeper problems. *Physical Review A*, 108(6):062423, 2023.

Arthur Pesah, Marco Cerezo, Samson Wang, Tyler Volkoff, Andrew T Sornborger, and Patrick J Coles. Absence of barren plateaus in quantum convolutional neural networks. *Physical Review X*, 11(4):041011, 2021.

Lirandë Pira and Chris Ferrie. An invitation to distributed quantum neural networks. *Quantum Machine Intelligence*, 5(2):1–24, 2023.

Christophe Piveteau and David Sutter. Circuit knitting with classical communication. *IEEE Transactions on Information Theory*, 2023.

Christophe Piveteau, David Sutter, and Stefan Woerner. Quasiprobability decompositions with reduced sampling overhead. *npj Quantum Information*, 8(1):12, 2022.

Rafika Rahmawati, Muhammad Taufiqi, Lila Yuwana, Agus Purwanto, and I Nengah Artawan. Encrypted broadcast quantum teleportation. *Physica Scripta*, 100(9):095118, 2025.

Ji-Gang Ren, Ping Xu, Hai-Lin Yong, Liang Zhang, Sheng-Kai Liao, Juan Yin, Wei-Yue Liu, Wen-Qi Cai, Meng Yang, Li Li, et al. Ground-to-satellite quantum teleportation. *Nature*, 549(7670):70–73, 2017.

Wenhui Ren, Weikang Li, Shibo Xu, Ke Wang, Wenjie Jiang, Feitong Jin, Xuhao Zhu, Jiachen Chen, Zixuan Song, Pengfei Zhang, et al. Experimental quantum adversarial learning with programmable superconducting qubits. *Nature Computational Science*, 2(11):711–717, 2022.

Daniel A Roberts and Beni Yoshida. Chaos and complexity by design. *Journal of High Energy Physics*, 2017(4):1–64, 2017.

Himanshu Sahu and Hari Prabhat Gupta. Nac-qfl: Noise aware clustered quantum federated learning. *arXiv preprint arXiv:2406.14236*, 2024.

Aman Saxena, Tom Wollschläger, Nicola Franco, Jeanette Miriam Lorenz, and Stephan Günnemann. Certifiably robust encoding schemes. In *Proceedings of the 5th IEEE International Conference on Quantum Computing and Engineering (QCE)*, volume 1, pages 1571–1582, 2024.

Lukas Schmitt, Christophe Piveteau, and David Sutter. Cutting circuits with multiple two-qubit unitaries. *arXiv preprint arXiv:2312.11638*, 2023.

Maria Schuld, Ville Bergholm, Christian Gogolin, Josh Izaac, and Nathan Killoran. Evaluating analytic gradients on quantum hardware. *Physical Review A*, 99(3):032331, 2019.

James R Seddon and Earl T Campbell. Quantifying magic for multi-qubit operations. *Proceedings of the Royal Society A*, 475(2227):20190251, 2019.

James R Seddon, Bartosz Regula, Hakop Pashayan, Yingkai Ouyang, and Earl T Campbell. Quantifying quantum speedups: Improved classical simulation from tighter magic monotones. *PRX Quantum*, 2(1):010345, 2021.

Philipp Seitz, Manuel Geiger, and Christian B Mendl. Multithreaded parallelism for heterogeneous clusters of qpus. In *Proceedings of the 39th International Supercomputing Conference (ISC) High Performance*, pages 1–8, 2024.

Yasuhiro Sekino and Leonard Susskind. Fast scramblers. *Journal of High Energy Physics*, 2008(10):065, 2008.

Ulrich Seyfarth. Cyclic mutually unbiased bases and quantum public-key encryption. *arXiv preprint arXiv:1907.02726*, 2019.

Aqsa Shabbir, Halil İbrahim Kanpak, Alptekin Küpçü, and Sinem Sav. A taxonomy of attacks and defenses in split learning. *arXiv preprint arXiv:2505.05872*, 2025.

Stephen H Shenker and Douglas Stanford. Black holes and the butterfly effect. *Journal of High Energy Physics*, 2014 (3):1–25, 2014.

Y-Y Shi, L-M Duan, and Guifre Vidal. Classical simulation of quantum many-body systems with a tree tensor network. *Physical Review A—Atomic, Molecular, and Optical Physics*, 74(2):022320, 2006.

Haozhen Situ, Zhimin He, Shenggen Zheng, and Lvzhou Li. Distributed quantum architecture search. *Physical Review A*, 110(2):022403, 2024.

Kaitlin N Smith, Michael A Perlin, Pranav Gokhale, Paige Frederick, David Owusu-Antwi, Richard Rines, Victory Omole, and Frederic Chong. Clifford-based circuit cutting for quantum simulation. In *Proceedings of the 50th Annual International Symposium on Computer Architecture (ISCA)*, pages 1–13, 2023.

Christian Szegedy, Wojciech Zaremba, Ilya Sutskever, Joan Bruna, Dumitru Erhan, Ian Goodfellow, and Rob Fergus. Intriguing properties of neural networks. *arXiv preprint arXiv:1312.6199*, 2013.

Luca Tagliacozzo, Glen Evenbly, and Guifré Vidal. Simulation of two-dimensional quantum systems using a tree tensor network that exploits the entropic area law. *Physical Review B—Condensed Matter and Materials Physics*, 80 (23):235127, 2009.

Wei Tang and Margaret Martonosi. Scaleqc: A scalable framework for hybrid computation on quantum and classical processors. *arXiv preprint arXiv:2207.00933*, 2022.

Wei Tang, Teague Tomesh, Martin Suchara, Jeffrey Larson, and Margaret Martonosi. Cutqc: Using small quantum computers for large quantum circuit evaluations. In *Proceedings of the 26th ACM International Conference on Architectural Support for Programming Languages and Operating Systems (ASPLOS)*, pages 473–486, 2021.

Kristan Temme, Sergey Bravyi, and Jay M Gambetta. Error mitigation for short-depth quantum circuits. *Physical review letters*, 119(18):180509, 2017.

Spyros Tserkis, Nedasadat Hosseinidehaj, Nathan Walk, and Timothy C Ralph. Teleportation-based collective attacks in gaussian quantum key distribution. *Physical Review Research*, 2(1):013208, 2020.

Gideon Uchehara, Tor M Aamodt, and Olivia Di Matteo. Rotation-inspired circuit cut optimization. In *Proceedings of the 3rd IEEE/ACM International Workshop on Quantum Computing Software (QCS)*, pages 50–56, 2022.

Christian Ufrecht, Maniraman Periyasamy, Sebastian Rietsch, Daniel D Scherer, Axel Plinge, and Christopher Mutschler. Cutting multi-control quantum gates with zx calculus. *Quantum*, 7:1147, 2023.

Christian Ufrecht, Laura S Herzog, Daniel D Scherer, Maniraman Periyasamy, Sebastian Rietsch, Axel Plinge, and Christopher Mutschler. Optimal joint cutting of two-qubit rotation gates. *Physical Review A*, 109(5):052440, 2024.

Anupama Unnikrishnan and Damian Markham. Authenticated teleportation and verification in a noisy network. *Physical Review A*, 102(4):042401, 2020.

Rodney Van Meter, Kae Nemoto, WJ Munro, and Kohei M Itoh. Distributed arithmetic on a quantum multicomputer. *ACM SIGARCH Computer Architecture News*, 34(2):354–365, 2006.

Praneeth Vepakomma, Otkrist Gupta, Tristan Swedish, and Ramesh Raskar. Split learning for health: Distributed deep learning without sharing raw patient data. *arXiv preprint arXiv:1812.00564*, 2018.

William M Watkins, Samuel Yen-Chi Chen, and Shinjae Yoo. Quantum machine learning with differential privacy. *Scientific Reports*, 13(1):2453, 2023.

John Watrous. *The Theory of Quantum Information*. Cambridge university press, 2018.

Maurice Weber, Nana Liu, Bo Li, Ce Zhang, and Zhikuan Zhao. Optimal provable robustness of quantum classification via quantum hypothesis testing. *npj Quantum Information*, 7(1):76, 2021.

Maxwell T West, Sarah M Erfani, Christopher Leckie, Martin Sevior, Lloyd CL Hollenberg, and Muhammad Usman. Benchmarking adversarially robust quantum machine learning at scale. *Physical Review Research*, 5(2):023186, 2023a.

Maxwell T West, Shu-Lok Tsang, Jia S Low, Charles D Hill, Christopher Leckie, Lloyd CL Hollenberg, Sarah M Erfani, and Muhammad Usman. Towards quantum enhanced adversarial robustness in machine learning. *Nature Machine Intelligence*, pages 1–9, 2023b.

Maxwell T West, Azar C Nakhl, Jamie Heredge, Floyd M Creevey, Lloyd CL Hollenberg, Martin Sevior, and Muhammad Usman. Drastic circuit depth reductions with preserved adversarial robustness by approximate encoding for quantum machine learning. *Intelligent Computing*, 3:0100, 2024.

David Winderl, Nicola Franco, and Jeanette Miriam Lorenz. Quantum neural networks under depolarization noise: Exploring white-box attacks and defenses. *Quantum Machine Intelligence*, 6(2):83, 2024.

Tom Wollschläger, Aman Saxena, Nicola Franco, Jeanette Miriam Lorenz, and Stephan Günnemann. Discrete randomized smoothing meets quantum computing. In *Proceedings of the 5th IEEE International Conference on Quantum Computing and Engineering (QCE)*, volume 1, pages 1535–1546, 2024.

William K Wootters and Brian D Fields. Optimal state-determination by mutually unbiased measurements. *Annals of Physics*, 191(2):363–381, 1989.

William K Wootters and Wojciech H Zurek. A single quantum cannot be cloned. *Nature*, 299(5886):802–803, 1982.

Qi Xia and Qun Li. Quantumfed: A federated learning framework for collaborative quantum training. In *Proceedings of the 2021 IEEE global communications conference (GLOBECOM)*, pages 1–6, 2021.

Qi Xia, Zeyi Tao, and Qun Li. Defending against byzantine attacks in quantum federated learning. In *Proceedings of the 17th International Conference on Mobility, Sensing and Networking (MSN)*, pages 145–152, 2021.

Han Xiao, Kashif Rasul, and Roland Vollgraf. Fashion-mnist: a novel image dataset for benchmarking machine learning algorithms. *arXiv preprint arXiv:1708.07747*, 2017.

Qichao Xu, Lifeng Zhao, Zhou Su, Dongfeng Fang, and Ruidong Li. Secure federated learning in quantum autonomous vehicular networks. *IEEE Network*, 37(6):240–247, 2023.

Fangchao Yu, Lina Wang, Bo Zeng, Kai Zhao, Zhi Pang, and Tian Wu. How to backdoor split learning. *Neural Networks*, 168:326–336, 2023.

Fangchao Yu, Bo Zeng, Kai Zhao, Zhi Pang, and Lina Wang. Chronic poisoning: Backdoor attack against split learning. In *Proceedings of the 38th Association for the Advancement of Artificial Intelligence Conference (AAAI)*, volume 38, pages 16531–16538, 2024.

Xiao Yuan, Jinzhao Sun, Junyu Liu, Qi Zhao, and You Zhou. Quantum simulation with hybrid tensor networks. *Physical Review Letters*, 127(4):040501, 2021.

Yichi Zhang, Chao Zhang, Cai Zhang, Lixin Fan, Bei Zeng, and Qiang Yang. Federated learning with quantum secure aggregation. *arXiv preprint arXiv:2207.07444*, 2022.

Li Zhou and Mingsheng Ying. Differential privacy in quantum computation. In *Proceedings of the 30th IEEE Computer Security Foundations Symposium (CSF)*, pages 249–262, 2017.

Mariam Zomorodi-Moghadam, Mahboobeh Houshmand, and Monireh Houshmand. Optimizing teleportation cost in distributed quantum circuits. *International Journal of Theoretical Physics*, 57(3):848–861, 2018.

Marek Zukowski, Anton Zeilinger, M Horne, and Artur Ekert. ”event-ready-detectors” bell experiment via entanglement swapping. *Physical review letters*, 71(26), 1993.

A Proof of Theorem 6.1

We use the following lemmata in our analysis.

Lemma A.1 (Subadditivity of diamond distance; Proposition 3.48 in (Watrous, 2018))**.** *For CPTP maps $\mathcal{A}$ and $\mathcal{C}$ from d-qubit to d'-qubit systems and CPTP maps $\mathcal{B}$ and $\mathcal{D}$ from d'-qubit to d''-qubit systems,*

$$\|\mathcal{AB} - \mathcal{CD}\|_\diamond \leq \|\mathcal{A} - \mathcal{C}\|_\diamond + \|\mathcal{B} - \mathcal{D}\|_\diamond.$$

Lemma A.2 (Diamond and operator distance of unitaries; Proposition I.6 in (Haah et al., 2023))**.** *For unitary channels $\mathcal{U}$ and $\mathcal{V}$ associated to unitary matrices $U, V \in U(d)$,*

$$\frac{1}{2}\|\mathcal{U} - \mathcal{V}\|_\diamond \leq \min_{\phi \in U(1)} \|\phi U - V\|_{op} \leq \|\mathcal{U} - \mathcal{V}\|_\diamond, \tag{16}$$

where $\mathcal{U}(.) = U(.)U^\dagger$, $\mathcal{V}(.) = V(.)V^\dagger$, and $\|.\|_\diamond$ and $\|.\|_{op}$ denote the diamond norm and operator norm, respectively. The intermediate term in (16) represents the distance between the unitary matrices up to a global phase.

With these in place, we are now prepared to proceed with the proof of Theorem 6.1.

Proof. Before delving into the proof, we define $\tilde{\mathcal{E}} := \hat{\mathcal{E}} \circ (\hat{\mathcal{U}}_0 \otimes \mathcal{I}^{\otimes d_a})$, where $\hat{\mathcal{U}}_0$ and $\mathcal{I}^{\otimes d_a}$ denote the unitary channel associated with $\hat{U}_0$ and the the identity channel acting on a d_a-qubit system, receptively. Using this definition, we have $\hat{\mathcal{E}}(\hat{U}_0 \sigma \hat{U}_0^\dagger \otimes |a\rangle\langle a|) = \tilde{\mathcal{E}}(\sigma \otimes |a\rangle\langle a|))$. To establish a bound on $|y_k(\sigma) - \hat{y}_k(\sigma)|$, we begin by deriving the following inequality.

$$\begin{aligned}
\|\mathcal{E}(\sigma \otimes |a\rangle\langle a|) - \hat{\mathcal{E}}(\hat{U}_0 \sigma \hat{U}_0^\dagger \otimes |a\rangle\langle a|))\|_1 &= \|\mathcal{E}(\sigma \otimes |a\rangle\langle a|) - \tilde{\mathcal{E}}(\sigma \otimes |a\rangle\langle a|))\|_1 \\
&\leq \sup_\rho \|(\mathcal{I}_R \otimes \mathcal{E})(\rho) - (\mathcal{I}_R \otimes \tilde{\mathcal{E}})(\rho)\|_1 \\
&= \|\mathcal{E} - \tilde{\mathcal{E}}\|_\diamond \\
&= \|\mathcal{E}_n \circ \cdots \circ \mathcal{E}_2 \circ \mathcal{E}_1 - \hat{\mathcal{U}}_n \circ \mathcal{E}_n \cdots \circ \hat{\mathcal{U}}_1 \circ \mathcal{E}_1 \circ (\hat{\mathcal{U}}_0 \otimes \mathcal{I}^{\otimes d})\|_\diamond \\
&\leq \|\mathcal{I}^{\otimes d_+} - \hat{\mathcal{U}}_0 \otimes \mathcal{I}^{\otimes d}\|_\diamond + \sum_{i=1}^n \|\mathcal{I}^{\otimes d_+} - \hat{\mathcal{U}}_i\|_\diamond \\
&\leq \|\mathcal{I}^{\otimes d} - \hat{\mathcal{U}}_0\|_\diamond + \sum_{i=1}^n \|\mathcal{I}^{\otimes d_+} - \hat{\mathcal{U}}_i\|_\diamond \\
&\leq 2\left(\min_{\phi_0 \in U(1)} \|I^{\otimes d} - \phi_0 \hat{U}_0\|_{op} + \sum_{i=1}^n \min_{\phi_i \in U(1)} \|I^{\otimes d_+} - \phi_i \hat{U}_i\|_{op}\right),
\end{aligned} \tag{17}$$

where $I^{\otimes d_+}$ represents the d_+-qubit identity operator and $\mathcal{I}^{\otimes d_+}$ denotes the associated identity channel. The second and third inequalities are due to Lemma A.1, while the forth inequality follows from Lemma A.2. To bound $|y_k(\sigma) - \hat{y}_k(\sigma)|$ using the above inequality, we use the following property (Nielsen and Chuang, 2010) of the trace distance, which can be derived using Hölder duality for Schatten norms. This property provides a physical interpretation of the trace distance, indicating that it represents the maximum possible difference in measurement outcome probabilities between two states, optimized over all measurement setups.

$$D(\rho_1, \rho_2) = \max_P \mathrm{Tr}[P(\rho_1 - \rho_2)],$$

where $D(\rho_1, \rho_2) = 1/2\|\rho_1 - \rho_2\|_1$ denotes the trace distance between two quantum states ρ_1 and ρ_2 and the maximization could be taken either over all projectors P or all positive operators such that $P \leq I$. Using this property, we have

$$\begin{aligned}
|y_k(\sigma) - \hat{y}_k(\sigma)| &= \left|\mathrm{Tr}(\Pi_k \mathcal{E}(\sigma \otimes |a\rangle\langle a|)) - \mathrm{Tr}(\Pi_k \hat{\mathcal{E}}(\hat{U}_0 \sigma \hat{U}_0^\dagger \otimes |a\rangle\langle a|))\right| \\
&= \left|\mathrm{Tr}\left(\Pi_k \left[\mathcal{E}(\sigma \otimes |a\rangle\langle a|) - \hat{\mathcal{E}}(\hat{U}_0 \sigma \hat{U}_0^\dagger \otimes |a\rangle\langle a|)\right]\right)\right| \\
&\leq \max_{0 \leq P \leq I} \mathrm{Tr}\left(P\left[\mathcal{E}(\sigma \otimes |a\rangle\langle a|) - \hat{\mathcal{E}}(\hat{U}_0 \sigma \hat{U}_0^\dagger \otimes |a\rangle\langle a|)\right]\right) \\
&= \frac{1}{2}\|\mathcal{E}(\sigma \otimes |a\rangle\langle a|) - \hat{\mathcal{E}}(\hat{U}_0 \sigma \hat{U}_0^\dagger \otimes |a\rangle\langle a|)\|_1
\end{aligned} \tag{18}$$

where P belongs to the set of positive operators and the inequality in line 3 follows from the property that $|x| \leq y$ if $x \leq y$ and $-x \leq y$ for two real numbers x and y. Combining (17) and (18) completes the proof. □

B Proof of Theorem 6.3

Proof. Using Chebyshev's inequality, for the random variable $y_k(\sigma) - \hat{y}_k(\sigma)$ and a real number $\delta > 0$, we have

$$\Pr\{|y_k(\sigma) - \hat{y}_k(\sigma) - \mathbb{E}_{W\sim\mu_{\mathbb{H}}}[y_k(\sigma) - \hat{y}_k(\sigma)]| \geq \delta\sqrt{\text{Var}(y_k(\sigma) - \hat{y}_k(\sigma))}\} \leq \frac{1}{\delta^2},$$

where $\text{Var}(y_k(\sigma) - \hat{y}_k(\sigma))$ denotes the variance. By replacing $\delta' = \delta\sqrt{\text{Var}(y_k(\sigma) - \hat{y}_k(\sigma))}$, we get:

$$\Pr\{|y_k(\sigma) - \hat{y}_k(\sigma) - \mathbb{E}_{W\sim\mu_{\mathbb{H}}}[y_k(\sigma) - \hat{y}_k(\sigma)]| \geq \delta'\} \leq \frac{\text{Var}(y_k(\sigma) - \hat{y}_k(\sigma))}{(\delta')^2}. \tag{19}$$

We can calculate the expected value as follows.

$$\begin{aligned}
\mathbb{E}_{W\sim\mu_{\mathbb{H}}}[y_k(\sigma) - \hat{y}_k(\sigma)] &= \mathbb{E}[\text{Tr}(\Pi_k\mathcal{E}(\sigma)) - \text{Tr}(\Pi_k\hat{\mathcal{E}}(\hat{U}_0\sigma\hat{U}_0^\dagger))] \\
&= \mathbb{E}[\text{Tr}(\mathcal{E}^\dagger(\Pi_k)\sigma) - \text{Tr}(\hat{\mathcal{E}}^\dagger(\Pi_k)\hat{U}_0\sigma\hat{U}_0^\dagger)] \\
&= \text{Tr}(\mathcal{E}^\dagger(\Pi_k)\mathbb{E}[\sigma]) - \text{Tr}(\hat{\mathcal{E}}^\dagger(\Pi_k)\mathbb{E}[\hat{U}_0\sigma\hat{U}_0^\dagger]) \\
&= \text{Tr}(\mathcal{E}^\dagger(\Pi_k)\mathbb{E}[\sigma]) - \text{Tr}(\hat{\mathcal{E}}^\dagger(\Pi_k)\mathbb{E}[\sigma]).
\end{aligned} \tag{20}$$

Here, $\mathcal{E}^\dagger$ and $\hat{\mathcal{E}}^\dagger$ denote the adjoints of the channels $\mathcal{E}$ and $\hat{\mathcal{E}}$, respectively. Line 4 is a result of the invariance of Haar measure under left and right multiplication by unitary matrices. By replacing $\mathbb{E}_{W\sim\mu_{\mathbb{H}}}[\sigma] = \mathbb{E}_{W\sim\mu_{\mathbb{H}}}[W\,|0\rangle\langle 0|\,W^\dagger] = (1/D)I$ in (20), where $D = 2^d$ denotes the dimension of the $D \times D$ unitary W and I is used, for simplicity, instead of $I^{\otimes d}$, we get

$$\mathbb{E}_{W\sim\mu_{\mathbb{H}}}[y_k(\sigma) - \hat{y}_k(\sigma)] = \frac{1}{D}\text{Tr}(\mathcal{E}^\dagger(\Pi_k)) - \frac{1}{D}\text{Tr}(\hat{\mathcal{E}}^\dagger(\Pi_k)). \tag{21}$$

It is straightforward to show $\hat{\mathcal{E}}^\dagger(.) = \mathcal{E}_1^\dagger \circ \hat{\mathcal{U}}_1^\dagger \cdots \circ \mathcal{E}_n^\dagger \circ \hat{\mathcal{U}}_n^\dagger(.)$. To see why, for two operators $A, B \in \mathcal{L}(\mathcal{H}^{\otimes d})$, we have:

$$\begin{aligned}
\text{Tr}(\hat{\mathcal{E}}^\dagger(A)B) =& \text{Tr}(A\hat{\mathcal{E}}(B)) \\
=& \text{Tr}(A(\hat{\mathcal{U}}_n \circ \mathcal{E}_n \cdots \circ \hat{\mathcal{U}}_1 \circ \mathcal{E}_1(B))) \\
=& \text{Tr}((\hat{\mathcal{U}}_n^\dagger(A))(\mathcal{E}_n \circ \hat{\mathcal{U}}_{n-1} \circ \mathcal{E}_{n-1} \cdots \circ \hat{\mathcal{U}}_1 \circ \mathcal{E}_1(B))) \\
=& \text{Tr}((\mathcal{E}_n^\dagger \circ \hat{\mathcal{U}}_n^\dagger(A))(\hat{\mathcal{U}}_{n-1} \circ \mathcal{E}_{n-1} \cdots \circ \hat{\mathcal{U}}_1 \circ \mathcal{E}_1(B))) \\
&\vdots \\
=& \text{Tr}((\mathcal{E}_1^\dagger \circ \hat{\mathcal{U}}_1^\dagger \cdots \circ \mathcal{E}_n^\dagger \circ \hat{\mathcal{U}}_n^\dagger(A))B).
\end{aligned}$$

Given the invariance of the trace under unitary operations, CPTP maps, and adjoints of unital maps, we have $\text{Tr}(\mathcal{E}^\dagger(\Pi_k)) = \text{Tr}(\Pi_k)$ and $\text{Tr}(\hat{\mathcal{E}}^\dagger(\Pi_k)) = \text{Tr}(\mathcal{E}_1^\dagger \circ \hat{\mathcal{U}}_1^\dagger \cdots \circ \mathcal{E}_n^\dagger \circ \hat{\mathcal{U}}_n^\dagger(\Pi_k)) = \text{Tr}(\Pi_k)$. Combining this with (21), we obtain

$$\mathbb{E}_{W\sim\mu_{\mathbb{H}}}[y_k(\sigma) - \hat{y}_k(\sigma)] = 0. \tag{22}$$

To determine the variance, we can expand the following expression and address each term separately.

$$\begin{aligned}
\text{Var}(y_k(\sigma) - \hat{y}_k(\sigma)) &= \mathbb{E}_{W\sim\mu_{\mathbb{H}}}[(y_k(\sigma) - \hat{y}_k(\sigma))^2] - \mathbb{E}_{W\sim\mu_{\mathbb{H}}}[y_k(\sigma) - \hat{y}_k(\sigma)]^2 \\
&= \mathbb{E}_{W\sim\mu_{\mathbb{H}}}[(y_k(\sigma) - \hat{y}_k(\sigma))^2] \\
&= \mathbb{E}_{W\sim\mu_{\mathbb{H}}}[y_k(\sigma)^2 + \hat{y}_k(\sigma)^2 - 2y_k(\sigma)\hat{y}_k(\sigma)] \\
&= \mathbb{E}_{W\sim\mu_{\mathbb{H}}}[(\text{Tr}(\Pi_k\mathcal{E}(\sigma)))^2 + (\text{Tr}(\Pi_k\hat{\mathcal{E}}(\hat{U}_0\sigma\hat{U}_0^\dagger)))^2 - 2\text{Tr}(\Pi_k\mathcal{E}(\sigma))\text{Tr}(\Pi_k\hat{\mathcal{E}}(\hat{U}_0\sigma\hat{U}_0^\dagger))].
\end{aligned} \tag{23}$$

Since $\text{Tr}(A)\text{Tr}(B) = \text{Tr}(A \otimes B)$ and $(AB) \otimes (A'B') = (A \otimes A')(B \otimes B')$ for operators A, B, A' and B', we have

$$(\text{Tr}(\Pi_k\mathcal{E}(\sigma)))^2 = (\text{Tr}(\mathcal{E}^\dagger(\Pi_k)\sigma))^2 = \text{Tr}(\mathcal{E}^\dagger(\Pi_k)\sigma \otimes \mathcal{E}^\dagger(\Pi_k)\sigma) = \text{Tr}((\mathcal{E}^\dagger(\Pi_k))^{\otimes 2}\sigma^{\otimes 2}).$$

Therefore,

$$\mathbb{E}_{W\sim\mu\mathbb{H}}[(\mathrm{Tr}(\Pi_k\mathcal{E}(\sigma)))^2] = \mathbb{E}_{W\sim\mu\mathbb{H}}[\mathrm{Tr}((\mathcal{E}^\dagger(\Pi_k))^{\otimes 2}\sigma^{\otimes 2})] = \mathrm{Tr}((\mathcal{E}^\dagger(\Pi_k))^{\otimes 2}\mathbb{E}[\sigma^{\otimes 2}]). \tag{24}$$

For an operator O acting on $\mathcal{H}\otimes\mathcal{H}$, the following holds (Roberts and Yoshida, 2017)

$$\begin{aligned}\mathbb{E}_{U\sim\mu\mathbb{H}}[U^\dagger\otimes U^\dagger O U\otimes U] &= \int_{U\sim\mu\mathbb{H}} U^\dagger\otimes U^\dagger O U\otimes U\,\mathrm{d}U \\ &= \frac{1}{D^2-1}\left(I\,\mathrm{Tr}[O] + S\,\mathrm{Tr}[SO] - \frac{1}{D}S\,\mathrm{Tr}[O] - \frac{1}{D}I\,\mathrm{Tr}[SO]\right),\end{aligned} \tag{25}$$

where S denotes the SWAP operator. Replacing O with $(|0\rangle\langle 0|)^{\otimes 2}$ in (25), we get

$$\begin{aligned}\mathbb{E}[\sigma^{\otimes 2}] &= \frac{1}{D^2-1}\left(I\,\mathrm{Tr}[(|0\rangle\langle 0|)^{\otimes 2}] + S\,\mathrm{Tr}[(|0\rangle\langle 0|)^2] - \frac{1}{D}S\,\mathrm{Tr}[(|0\rangle\langle 0|)^{\otimes 2}] - \frac{1}{D}I\,\mathrm{Tr}[(|0\rangle\langle 0|)^2]\right) \\ &= \frac{1}{D^2-1}(1-\frac{1}{D})(I+S) = \frac{I+S}{D(D+1)},\end{aligned} \tag{26}$$

where we used the property that $\mathrm{Tr}(S\rho\otimes\rho) = \mathrm{Tr}(\rho^2)$ for a density operator ρ. Combining (24) and (26), we get:

$$\mathbb{E}_{W\sim\mu\mathbb{H}}[(\mathrm{Tr}(\Pi_k\mathcal{E}(\sigma)))^2] = \frac{1}{D(D+1)}\left(\mathrm{Tr}((\mathcal{E}^\dagger(\Pi_k))^{\otimes 2}) + \mathrm{Tr}((\mathcal{E}^\dagger(\Pi_k))^2)\right). \tag{27}$$

We define $\tilde{\mathcal{E}} := \hat{\mathcal{E}}\circ\hat{\mathcal{U}}_0$. Similar to (27), we can show

$$\mathbb{E}_{W\sim\mu\mathbb{H}}[(\mathrm{Tr}(\Pi_k\hat{\mathcal{E}}(\hat{U}_0\sigma\hat{U}_0^\dagger)))^2] = \mathbb{E}_{W\sim\mu\mathbb{H}}[(\mathrm{Tr}(\Pi_k\tilde{\mathcal{E}}(\sigma)))^2] = \frac{1}{D(D+1)}\left(\mathrm{Tr}((\tilde{\mathcal{E}}^\dagger(\Pi_k))^{\otimes 2}) + \mathrm{Tr}((\tilde{\mathcal{E}}^\dagger(\Pi_k))^2)\right). \tag{28}$$

For the third term in (23), we have:

$$\begin{aligned}-2\mathrm{Tr}(\Pi_k\mathcal{E}(\sigma))\mathrm{Tr}(\Pi_k\hat{\mathcal{E}}(\hat{U}_0\sigma\hat{U}_0^\dagger)) &= -2\mathrm{Tr}(\Pi_k\mathcal{E}(\sigma))\mathrm{Tr}(\Pi_k\tilde{\mathcal{E}}(\sigma)) \\ &= -2\mathrm{Tr}(\mathcal{E}^\dagger(\Pi_k)\sigma)\mathrm{Tr}(\tilde{\mathcal{E}}^\dagger(\Pi_k)\sigma) \\ &= -2\mathrm{Tr}(\mathcal{E}^\dagger(\Pi_k)\sigma\otimes\tilde{\mathcal{E}}^\dagger(\Pi_k)\sigma) \\ &= -2\mathrm{Tr}((\mathcal{E}^\dagger(\Pi_k)\otimes\tilde{\mathcal{E}}^\dagger(\Pi_k))\sigma^{\otimes 2}),\end{aligned}$$

Taking the expectation of both sides gives us:

$$\begin{aligned}\mathbb{E}_{W\sim\mu\mathbb{H}}[-2\mathrm{Tr}(\Pi_k\mathcal{E}(\sigma))\mathrm{Tr}(\Pi_k\hat{\mathcal{E}}(\hat{U}_0\sigma\hat{U}_0^\dagger))] &= \mathbb{E}_{W\sim\mu\mathbb{H}}[-2\mathrm{Tr}((\mathcal{E}^\dagger(\Pi_k)\otimes\tilde{\mathcal{E}}^\dagger(\Pi_k))\sigma^{\otimes 2})] \\ &= -2\mathrm{Tr}((\mathcal{E}^\dagger(\Pi_k)\otimes\tilde{\mathcal{E}}^\dagger(\Pi_k))\mathbb{E}[\sigma^{\otimes 2}]).\end{aligned} \tag{29}$$

Utilizing (26) and (29), we obtain

$$\mathbb{E}_{W\sim\mu\mathbb{H}}[-2\mathrm{Tr}(\Pi_k\mathcal{E}(\sigma))\mathrm{Tr}(\Pi_k\hat{\mathcal{E}}(\hat{U}_0\sigma\hat{U}_0^\dagger))] = \frac{-2}{D(D+1)}\left(\mathrm{Tr}(\mathcal{E}^\dagger(\Pi_k)\otimes\tilde{\mathcal{E}}^\dagger(\Pi_k)) + \mathrm{Tr}(\mathcal{E}^\dagger(\Pi_k)\tilde{\mathcal{E}}^\dagger(\Pi_k))\right). \tag{30}$$

By combining (23) with (27), (28), and (30), we get

$$\begin{aligned}\mathrm{Var}(y_k(\sigma)-\hat{y}_k(\sigma)) = \frac{1}{D(D+1)}\Big[&\mathrm{Tr}((\mathcal{E}^\dagger(\Pi_k))^{\otimes 2}) + \mathrm{Tr}((\mathcal{E}^\dagger(\Pi_k))^2) + \mathrm{Tr}((\tilde{\mathcal{E}}^\dagger(\Pi_k))^{\otimes 2}) + \mathrm{Tr}((\tilde{\mathcal{E}}^\dagger(\Pi_k))^2) \\ &- 2\left(\mathrm{Tr}(\mathcal{E}^\dagger(\Pi_k)\otimes\tilde{\mathcal{E}}^\dagger(\Pi_k)) + \mathrm{Tr}(\mathcal{E}^\dagger(\Pi_k)\tilde{\mathcal{E}}^\dagger(\Pi_k))\right)\Big].\end{aligned}$$

By rearranging the terms, we have

$$\begin{aligned}\mathrm{Var}(y_k(\sigma)-\hat{y}_k(\sigma)) = \frac{1}{D(D+1)}\Big[&\mathrm{Tr}((\mathcal{E}^\dagger(\Pi_k))^{\otimes 2}) + \mathrm{Tr}((\tilde{\mathcal{E}}^\dagger(\Pi_k))^{\otimes 2}) - 2\mathrm{Tr}(\mathcal{E}^\dagger(\Pi_k)\otimes\tilde{\mathcal{E}}^\dagger(\Pi_k)) \\ &+ \mathrm{Tr}((\mathcal{E}^\dagger(\Pi_k))^2) + \mathrm{Tr}((\tilde{\mathcal{E}}^\dagger(\Pi_k))^2) - 2\mathrm{Tr}(\mathcal{E}^\dagger(\Pi_k)\tilde{\mathcal{E}}^\dagger(\Pi_k))\Big].\end{aligned}$$

By replacing $\text{Tr}((\mathcal{E}^\dagger(\Pi_k))^{\otimes 2})$ with $(\text{Tr}(\mathcal{E}^\dagger(\Pi_k)))^2$, $\text{Tr}((\tilde{\mathcal{E}}^\dagger(\Pi_k))^{\otimes 2})$ with $(\text{Tr}(\tilde{\mathcal{E}}^\dagger(\Pi_k)))^2$, and $-2\text{Tr}(\mathcal{E}^\dagger(\Pi_k)\otimes\tilde{\mathcal{E}}^\dagger(\Pi_k))$ with $-2\text{Tr}(\mathcal{E}^\dagger(\Pi_k))\text{Tr}(\tilde{\mathcal{E}}^\dagger(\Pi_k))$, we obtain

$$\begin{aligned}\text{Var}(y_k(\sigma)-\hat{y}_k(\sigma)) = \frac{1}{D(D+1)}\Big[&(\text{Tr}(\mathcal{E}^\dagger(\Pi_k))-\text{Tr}(\tilde{\mathcal{E}}^\dagger(\Pi_k)))^2 \\ &+\text{Tr}((\mathcal{E}^\dagger(\Pi_k))^2)+\text{Tr}((\tilde{\mathcal{E}}^\dagger(\Pi_k))^2)-2\text{Tr}(\mathcal{E}^\dagger(\Pi_k)\tilde{\mathcal{E}}^\dagger(\Pi_k))\Big].\end{aligned}$$

As we previously argued, $\text{Tr}(\mathcal{E}^\dagger(\Pi_k))=\text{Tr}(\tilde{\mathcal{E}}^\dagger(\Pi_k))=\text{Tr}(\Pi_k)$. Therefore, $(\text{Tr}(\mathcal{E}^\dagger(\Pi_k))-\text{Tr}(\tilde{\mathcal{E}}^\dagger(\Pi_k)))^2=0$, and

$$\begin{aligned}\text{Var}(y_k(\sigma)-\hat{y}_k(\sigma)) &= \frac{1}{D(D+1)}\Big[\text{Tr}((\mathcal{E}^\dagger(\Pi_k))^2)+\text{Tr}((\tilde{\mathcal{E}}^\dagger(\Pi_k))^2)-2\text{Tr}(\mathcal{E}^\dagger(\Pi_k)\tilde{\mathcal{E}}^\dagger(\Pi_k))\Big] \\ &= \frac{1}{D(D+1)}\text{Tr}\left((\mathcal{E}^\dagger(\Pi_k))^2+(\tilde{\mathcal{E}}^\dagger(\Pi_k))^2-2\mathcal{E}^\dagger(\Pi_k)\tilde{\mathcal{E}}^\dagger(\Pi_k)\right) \\ &= \frac{1}{D(D+1)}\text{Tr}\left((\mathcal{E}^\dagger(\Pi_k)-\tilde{\mathcal{E}}^\dagger(\Pi_k))^2\right).\end{aligned}$$

Since Π_k is Hermitian and adjoints of CPTP maps preserve Hermiticity, $(\mathcal{E}^\dagger(\Pi_k)-\tilde{\mathcal{E}}^\dagger(\Pi_k))^2 = (\mathcal{E}^\dagger(\Pi_k)-\tilde{\mathcal{E}}^\dagger(\Pi_k))^\dagger(\mathcal{E}^\dagger(\Pi_k)-\tilde{\mathcal{E}}^\dagger(\Pi_k))$, and

$$\begin{aligned}\text{Var}(y_k(\sigma)-\hat{y}_k(\sigma)) &= \frac{1}{D(D+1)}\text{Tr}\left((\mathcal{E}^\dagger(\Pi_k)-\tilde{\mathcal{E}}^\dagger(\Pi_k))^\dagger(\mathcal{E}^\dagger(\Pi_k)-\tilde{\mathcal{E}}^\dagger(\Pi_k))\right) \\ &= \frac{1}{D(D+1)}D_{HS}(\mathcal{E}^\dagger(\Pi_k),\tilde{\mathcal{E}}^\dagger(\Pi_k))^2,\end{aligned} \tag{31}$$

where D_{HS} denotes the Hilbert-Schmidt distance. We can bound this distance as follows.

$$\begin{aligned}D_{HS}(\mathcal{E}^\dagger(\Pi_k),\tilde{\mathcal{E}}^\dagger(\Pi_k)) =& D_{HS}(\mathcal{E}_1^\dagger\circ\mathcal{E}_2^\dagger\cdots\circ\mathcal{E}_n^\dagger(\Pi_k),\hat{\mathcal{U}}_0^\dagger\circ\mathcal{E}_1^\dagger\circ\hat{\mathcal{U}}_1^\dagger\cdots\circ\mathcal{E}_n^\dagger\circ\hat{\mathcal{U}}_n^\dagger(\Pi_k)) \\ =& \|\mathcal{E}_1^\dagger\circ\mathcal{E}_2^\dagger\cdots\circ\mathcal{E}_n^\dagger(\Pi_k)-\hat{\mathcal{U}}_0^\dagger\circ\mathcal{E}_1^\dagger\circ\hat{\mathcal{U}}_1^\dagger\cdots\circ\mathcal{E}_n^\dagger\circ\hat{\mathcal{U}}_n^\dagger(\Pi_k)\|_2 \\ =& \|\mathcal{E}_1^\dagger\circ\cdots\circ\mathcal{E}_n^\dagger(\Pi_k)-\hat{U}_0^\dagger(\mathcal{E}_1^\dagger\circ\cdots\circ\mathcal{E}_n^\dagger\circ\hat{\mathcal{U}}_n^\dagger(\Pi_k))\hat{U}_0\|_2 \\ =& \|\mathcal{E}_1^\dagger\circ\cdots\circ\mathcal{E}_n^\dagger(\Pi_k)-\hat{U}_0^\dagger(\mathcal{E}_1^\dagger\circ\cdots\circ\mathcal{E}_n^\dagger(\Pi_k)) \\ &+\hat{U}_0^\dagger(\mathcal{E}_1^\dagger\circ\cdots\circ\mathcal{E}_n^\dagger(\Pi_k))-\hat{U}_0^\dagger(\mathcal{E}_1^\dagger\circ\cdots\circ\mathcal{E}_n^\dagger\circ\hat{\mathcal{U}}_n^\dagger(\Pi_k))\hat{U}_0\|_2 \\ \leq& \|\mathcal{E}_1^\dagger\circ\cdots\circ\mathcal{E}_n^\dagger(\Pi_k)-\hat{U}_0^\dagger(\mathcal{E}_1^\dagger\circ\cdots\circ\mathcal{E}_n^\dagger(\Pi_k))\|_2 \\ &+\|\hat{U}_0^\dagger(\mathcal{E}_1^\dagger\circ\cdots\circ\mathcal{E}_n^\dagger(\Pi_k))-\hat{U}_0^\dagger(\mathcal{E}_1^\dagger\circ\cdots\circ\mathcal{E}_n^\dagger\circ\hat{\mathcal{U}}_n^\dagger(\Pi_k))\hat{U}_0\|_2 \\ \leq& \|I-\hat{U}_0^\dagger\|_2\|\mathcal{E}_1^\dagger\circ\cdots\circ\mathcal{E}_n^\dagger(\Pi_k)\|_2 \\ &+\|\mathcal{E}_1^\dagger\circ\cdots\circ\mathcal{E}_n^\dagger(\Pi_k)-(\mathcal{E}_1^\dagger\circ\cdots\circ\mathcal{E}_n^\dagger\circ\hat{\mathcal{U}}_n^\dagger(\Pi_k))\hat{U}_0\|_2 \\ \leq& \|I-\hat{U}_0^\dagger\|_2\|\Pi_k\|_2 \\ &+\|\mathcal{E}_1^\dagger\circ\cdots\circ\mathcal{E}_n^\dagger(\Pi_k)-(\mathcal{E}_1^\dagger\circ\cdots\circ\mathcal{E}_n^\dagger\circ\hat{\mathcal{U}}_n^\dagger(\Pi_k))\hat{U}_0\|_2,\end{aligned} \tag{32}$$

where $\|.\|_2$ denotes Schatten 2-norm (also called the Hilbert-Schmidt norm). The first inequality is a result of the triangle inequality. The second inequality follows from the sub-multiplicative property of the Schatten 2-norm and its invariance under unitary transformations. The third inequality above holds because the Schatten 2-norm is contractive under the adjoint

of unital CPTP maps. We can bound the second term in (32) using a similar approach:

$$\begin{aligned}
&\|\mathcal{E}_1^\dagger \circ \cdots \circ \mathcal{E}_n^\dagger(\Pi_k) - (\mathcal{E}_1^\dagger \circ \cdots \circ \mathcal{E}_n^\dagger \circ \hat{\mathcal{U}}_n^\dagger(\Pi_k))\hat{U}_0\|_2 \\
=&\|\mathcal{E}_1^\dagger \circ \cdots \circ \mathcal{E}_n^\dagger(\Pi_k) - (\mathcal{E}_1^\dagger \circ \cdots \circ \mathcal{E}_n^\dagger(\Pi_k))\hat{U}_0 \\
&+ (\mathcal{E}_1^\dagger \circ \cdots \circ \mathcal{E}_n^\dagger(\Pi_k))\hat{U}_0 - (\mathcal{E}_1^\dagger \circ \cdots \circ \mathcal{E}_n^\dagger \circ \hat{\mathcal{U}}_n^\dagger(\Pi_k))\hat{U}_0\|_2 \\
\leq&\|(\mathcal{E}_1^\dagger \circ \cdots \circ \mathcal{E}_n^\dagger(\Pi_k))(I - \hat{U}_0)\|_2 \\
&+ \|(\mathcal{E}_1^\dagger \circ \cdots \circ \mathcal{E}_n^\dagger(\Pi_k) - \mathcal{E}_1^\dagger \circ \cdots \circ \mathcal{E}_n^\dagger \circ \hat{\mathcal{U}}_n^\dagger(\Pi_k))\hat{U}_0\|_2 \\
\leq&\|(\mathcal{E}_1^\dagger \circ \cdots \circ \mathcal{E}_n^\dagger(\Pi_k))\|_2 \|I - \hat{U}_0\|_2 \\
&+ \|\mathcal{E}_1^\dagger \circ \cdots \circ \mathcal{E}_n^\dagger(\Pi_k) - \mathcal{E}_1^\dagger \circ \cdots \circ \mathcal{E}_n^\dagger \circ \hat{\mathcal{U}}_n^\dagger(\Pi_k)\|_2 \\
\leq&\|\Pi_k\|_2 \|I - \hat{U}_0\|_2 \\
&+ D_{HS}(\mathcal{E}_1^\dagger \circ \cdots \circ \mathcal{E}_n^\dagger(\Pi_k), \mathcal{E}_1^\dagger \circ \cdots \circ \mathcal{E}_n^\dagger \circ \hat{\mathcal{U}}_n^\dagger(\Pi_k))
\end{aligned} \tag{33}$$

Note that, $\|I - \hat{U}_0\|_2 = \|I - \hat{U}_0^\dagger\|_2$ since the Schatten 2-norm of an operator is the same as the Schatten 2-norm of its adjoint. Combining (32) and (33), we have

$$\begin{aligned}
D_{HS}(\mathcal{E}^\dagger(\Pi_k), \tilde{\mathcal{E}}^\dagger(\Pi_k)) &\leq 2\|I - \hat{U}_0\|_2 \|\Pi_k\|_2 + D_{HS}(\mathcal{E}_1^\dagger \circ \cdots \circ \mathcal{E}_n^\dagger(\Pi_k), \mathcal{E}_1^\dagger \circ \hat{\mathcal{U}}_1^\dagger \circ \cdots \circ \mathcal{E}_n^\dagger \circ \hat{\mathcal{U}}_n^\dagger(\Pi_k)) \\
&\leq 2\|I - \hat{U}_0\|_2 \|\Pi_k\|_2 + D_{HS}(\mathcal{E}_2^\dagger \circ \cdots \circ \mathcal{E}_n^\dagger(\Pi_k), \hat{\mathcal{U}}_1^\dagger \circ \mathcal{E}_2^\dagger \circ \cdots \circ \mathcal{E}_n^\dagger \circ \hat{\mathcal{U}}_n^\dagger(\Pi_k)),
\end{aligned}$$

where the second inequality holds since the Schatten 2-norm is contractive under the adjoint of unital CPTP maps. It is straightforward to inductively show

$$D_{HS}(\mathcal{E}^\dagger(\Pi_k), \tilde{\mathcal{E}}^\dagger(\Pi_k)) \leq 2\|\Pi_k\|_2 \left(\sum_{i=0}^{n} \|I - \hat{U}_i\|_2 \right). \tag{34}$$

By combining (19) and (22) with (31) and (34), we get

$$\begin{aligned}
\Pr\{|y_k(\sigma) - \hat{y}_k(\sigma)| \geq \delta'\} &\leq \frac{D_{HS}(\mathcal{E}^\dagger(\Pi_k), \tilde{\mathcal{E}}^\dagger(\Pi_k))^2}{D(D+1)(\delta')^2} \\
&\leq \frac{4\|\Pi_k\|_2^2 \left(\sum_{i=0}^{n} \|I - \hat{U}_i\|_2 \right)^2}{D(D+1)(\delta')^2}.
\end{aligned}$$

This completes the proof. □

C Experimental Results

C.1 Model Architecture

We employ parametrized quantum circuit (PQC)-based classifiers using hardware-efficient ansätze (Kandala et al., 2017) composed of ℓ layers, with each layer including a rotation unit and an entangling unit. Each rotation unit consists of single-qubit rotation gates with three trainable parameters: $Rot(\omega_1, \omega_2, \omega_3) = RZ(\omega_1) \cdot RY(\omega_2) \cdot RZ(\omega_3)$. Each entangling layer is structured such that the qubits are sequentially interconnected in a cyclic manner. Specifically, qubit i is entangled with qubit $i+1$ for $i = 1, 2, \ldots, (d_+) - 1$ using CNOT gates, and the final qubit, d_+, is entangled with the first qubit, 1, thereby forming a closed loop of entanglements. Recall that $d_+ = d + d_a$ denotes the total number of qubits in the classifier. We employ amplitude encoding to map classical data into a quantum state. Consequently, $d = \lceil \log_2 c \rceil$ qubits are required to represent c-dimensional classical data. For K-class classification, each classifier includes $d_a = \lceil \log_2 K \rceil$ ancilla bits initialized to $|0\rangle$[5]. Fig. 7 shows a classifier with adversarial layers implemented within its intermediate layers. We begin by training the classifier without any adversarial layers. Once the classifier is trained, we freeze its weights, add the desired adversarial layers based on our different experimental settings, and then train only the new layers. The adversarial layers have a similar architecture to the classifier's layer, with CNOT gates replaced by controlled phase-shift gates $CRZ(\phi)$ that apply a phase shift of angle ϕ to the target qubit around the Z-axis when the control qubit is in the $|1\rangle$ state. When ϕ is set to zero, this controlled gate behaves as an identity gate, irrespective of the control qubit's state. This allows us to initially set the adversarial layers to function as identity gates, and observe their impact on the model's performance as we train them.

[5]The number of ancilla bits is inspired by the settings used by Anil et al. (2024).

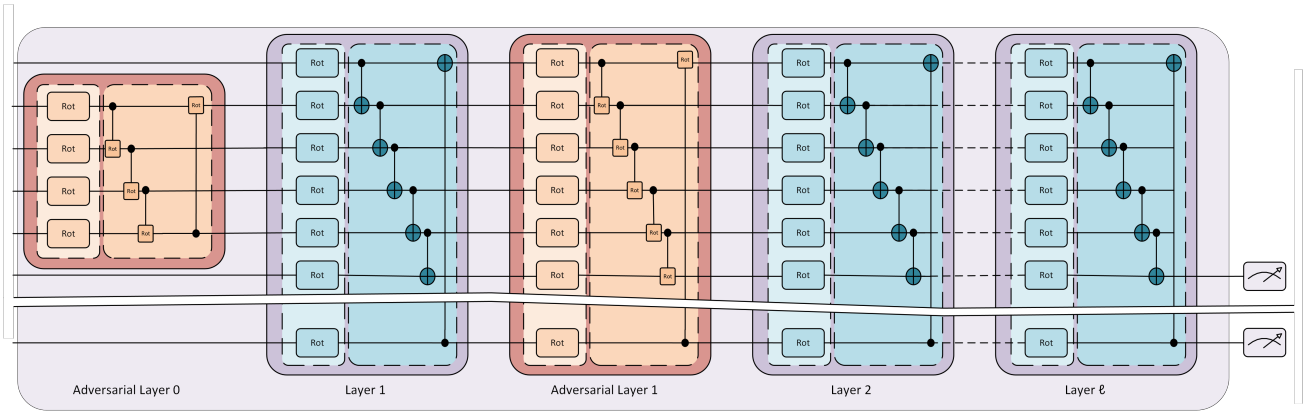
Rot
Rot
Rot

architectures such as tree tensor networks and quantum convolutional neural networks (QCNNs) (Cong et al., 2019) that are free of barren plateaus (Pesah et al., 2021; Miao and Barthel, 2024) can be classically simulable in polynomial time by a classical algorithm augmented by classical shadows (Cerezo et al., 2023; Bermejo et al., 2024). Therefore, one might consider these ansätze suboptimal choices for a quantum classifier. We chose strongly entangled classifiers for our experiments as they are widely used and allow us to investigate the robustness to adversarial unitaries inserted at different depths in classifiers that maintain a consistent number of qubits across all layers, preserving dimensionality throughout their depth.

C.2 Classifiers' Performance

Table 1 summarizes the classifiers' performance for MNIST and FMNIST before they are subjected to adversarial attacks. The classifiers are trained with depths of 10 and 20 for binary classification, and with depths of 20 and 40 for four-class classification. For binary classification, classes 0 and 1 from both the MNIST and FMNIST datasets are used, while for four-class classification, classes 0, 1, 2, and 3 from both datasets are utilized. In the FMNIST dataset, these classes correspond to images of T-shirts/tops, trousers, pullovers, and dresses. The models are trained with the Adam optimizer (Kingma and Ba, 2017) and a batch size of 64 for 5 epochs with a learning rate of 0.001, followed by 5 epochs with a learning rate of 0.0001 for binary classification. For four-class classification, they are trained for 30 epochs, with learning rates 0.001, 0.0001, and 0.00001 used during the first, middle, and final 10 epochs, respectively. Some of the settings here, such as the choice of classes from MNIST and FMNIST for binary and four-class training, the optimizer, batch size, number of epochs, and learning rates, are inspired by the settings employed by Anil et al. (2024).

Table 1: Test accuracy comparison across model depths for binary and multi-class classification on MNIST and FMNIST datasets.

	MNIST		FMNIST	
Number of layers	Binary	Four-class	Binary	Four-class
10	99.67%	-	94.80%	-
20	99.86%	90.40%	94.75%	79.80%
40	-	92.18%	-	84.18%

For CIFAR-10, inspired by the settings used by Winderl et al. (2024), the classifier is trained only for binary classification between classes zero and nine. We refer to this two-class subset as CIFAR-2. The images are resized from $32 \times 32 \times 3$ to 64×64, after which histogram of oriented gradients (HOG) features are extracted using 8×8 pixel cells and an inner block size of 1×1 cells, resulting in a 576-dimensional feature vector. We employ a classifier with depth 80, trained using Adam optimizer for 40 epochs with a learning rate of 0.0005 and a batch size of 64. Our model achieves a test accuracy of 83.05%.

C.3 Adversarial Attacks

Here, we examine the robustness of the classifiers with different depths to adversarial perturbations targeting their intermediate layers.

C.3.1 Attack Scenarios and Parameters

C.3.1.1 Global and Local Adversarial Layers: We explore three different scenarios for the number of qubits on which the adversarial layers can act. In the first settings, we assume the adversarial layers can impact all the qubits in the circuit, similar to adversarial layer 1 in Fig. 7, and study the effects of adding one or more blocks of such layers to the architecture. In the other two settings, the adversarial layers are restricted to acting only on local qubits, similar to adversarial layer 0 in Fig. 7. In the two settings where we study local adversarial gates, we consider gates acting on either three or four qubits. For each setting, we select a random block of consecutive qubits on which the adversarial gates act: three neighboring qubits for the three-qubit gates, and four neighboring qubits for the four-qubit gates. To ensure consistency across all experiments, we fix these selections: all three-qubit adversarial gates act on qubits $3, 4, 5$, and all four-qubit gates act on qubits $5, 6, 7, 8$.

C.3.1.2 Single versus Multiple Adversarial Layers: For all three scenarios described above, our goal is to compare the effects of adding a single block of adversarial layers to different depths, as well as incorporating multiple blocks into the model's architecture. For the case where a single block of adversarial layers is inserted within the layers of the classifier's circuit, we consider four scenarios. In the first, an adversarial block is inserted between the input and the first layer of

the circuit, perturbing the classifier's input state. In the second, an adversarial block is added between the $\lceil \ell/4 \rceil-$th and $(\lceil \ell/4 \rceil + 1)-$th layers, where ℓ denotes the number of classifier's layers. The third scenario involves inserting an adversarial block after the $\lceil \ell/2 \rceil-$th layer, before the $(\lceil \ell/2 \rceil + 1)-$th. Finally, in the fourth scenario, an adversarial block is introduced after the $\lceil 3(\ell/4) \rceil-$th layer, just before the $(\lceil 3(\ell/4) \rceil + 1)-$th. We compare the effects of these adversarial blocks with the simultaneous insertion of three blocks in place of those described in the second, third, and fourth scenarios. Regarding the scenario in which the adversarial layers can act on all qubits and are inserted between the input and the first layer of the circuit, note that in Equation (4) and in earlier sections of the paper, we assume an adversarial unitary perturbing the input state does not affect the ancilla bits. This assumption is made to align with prior literature in this area, which often assumes that the ancillary bits remain unaffected. However, in our experiments, we assume that the adversarial block of layers between the input and the first layer acts on all qubits in a manner similar to the other adversarial blocks examined, in order to maintain consistency. Note that the analysis in Section 6 could be easily extended to a scenario where U_0 also affects the ancilla bits.

C.3.1.3 Training the Adversarial Layers: Consider a quantum classifier with multiple adversarial gates within its intermediate layers, similar to the one shown in Fig. 2.(c), where the classifier is trained, but the adversarial gates have not been trained yet and act as identity gates. Let $\hat{\theta}$ denote the parameters the adversarial unitaries $\{\hat{U}_i\}_{i=0}^{n}$ depend on. Our experiments focus on untargeted attacks (see Section 3.3). Therefore, our objective is to train $\hat{\theta}$ using an optimization criterion similar to the one presented in (7). We employ an iterative process that progressively refines the adversarial unitaries to increase their effectiveness. To control the strength of the attack, i.e., the sum of the distances between the perturbation operators and the identity operator, we employ a constraint-based loss function. Following our analysis in Section 6, one possible approach involves using the Hilbert-Schmidt norm:

$$(\hat{U}_0, \hat{U}_1, \cdots, \hat{U}_n) = \underset{\hat{\theta}}{\operatorname{argmax}} \left(L(\hat{y}(\sigma_i), Y(\sigma_i)) + \gamma \sum_{i=1} \|I - \hat{U}_i\|_2 \right),$$

where γ is a hyperparameter controlling the trade-off between the attack's strength and its effectiveness. However, when $\hat{\theta}$ represents a weights matrix, it is possible to opt for a simpler yet practically effective method, which relies on adding $\|\hat{\theta}\|_{\ell_2}$ to the optimization objective, with $||.||_{\ell_2}$ denoting the ℓ_2-norm:

$$(\hat{U}_0, \cdots, \hat{U}_n) = \underset{\hat{\theta}}{\operatorname{argmax}} \left(L(\hat{y}(\sigma_i), Y(\sigma_i)) + \gamma \|\hat{\theta}\|_{\ell_2} \right), \tag{35}$$

where for the loss function L in our experiments, we employ the cross-entropy loss function, which is the same loss function used to train our classifiers before subjecting them to adversarial attacks. Using this optimization objective eliminates the need to calculate the Hilbert-Schmidt distances between the perturbation operators and the identity operator during training, resulting in a more computationally efficient training process.

We consider a white-box setting, where the adversary has complete knowledge of the target classifier. To train the adversarial layers, we freeze the classifier's weights, and employ a loss function similar to (35). Since each single-qubit rotation gate requires three trainable parameters and each controlled phase-shift gate needs one trainable parameter, for a circuit with ℓ_{adv} adversarial layers, the trainable parameters can be represented by a $d_{adv} \times \ell_{adv} \times 4$ matrix, where d_{adv} is the number of qubits the adversarial layers act on. We employ the ℓ_2 norm of this matrix in place of $\|\hat{\theta}\|_2$ in (35). The trainable parameters are initialized to zero before training begins, causing the adversarial layers to behave as identity operators initially.

C.3.1.4 Evaluating the Adversarial Attacks: To evaluate the effectiveness of the adversarial layers in causing incorrect predictions for each classifier, we compare the misclassification rates across different scenarios. Specifically, we record the misclassification rate and the corresponding attack strength at each epoch during the training of each adversarial scenario, plotting the misclassification rate versus attack strength to analyze their relationship over time. This visualization helps identify the strength levels needed to maximize misclassification for each attack, facilitating comparisons of attack efficiency and convergence dynamics across different scenarios. Here, by misclassification rate, we refer to the percentage of incorrect predictions made by the attacked classifier after each epoch, when evaluated on the entire test set. Furthermore, to evaluate the attack strength, we use the sum of the normalized Hilbert Schmidt distances between the adversarial unitaries inserted into the architecture and the identity operator: $\left(1/\sqrt{2^{d_{adv}}}\right) \sum_{i=0}^{n} ||\hat{U}_i - I^{\otimes d_{adv}}||_2$, where n denotes the total number of adversarial unitaries, and each $\hat{U}_i \in U(2^{d_{adv}})$. Normalizing the distance prevents larger operators from artificially dominating the metric due to their size.

C.3.1.5 Hyperparameters for Training the Adversarial Layers: For MNIST and FMNIST, when inserting a single adversarial unitary operator into the architecture, we use a block consisting of 10 adversarial layers in all our experiments. As explained earlier, we compare the effect of adding one adversarial unitary operator versus simultaneously inserting three adversarial unitaries into the circuits. When three unitaries are inserted, we consider two scenarios: In the first, the three adversarial unitaries consist of 3, 3, and 4 adversarial layers, respectively, resulting in a total of 10 layers. In the second scenario, each adversarial unitary consists of 10 layers. For CIFAR-2, when inserting a single unitary operator, we conduct experiments with two configurations: one in which the unitary consists of 10 layers and another in which it consists of 40 layers. This choice is motivated by the fact that the classifier used for CIFAR-2 is deeper than those used for MNIST and FMNIST. Therefore, we aim to examine whether an increased number of adversarial layers can have a greater impact on the model. The parameter γ in (35) controls whether the attack strength (i.e., the sum of the normalized Hilbert Schmidt distances) is allowed to increase significantly during training. In our experiments, we set $\gamma = 0$. As explained in Section $C.3.5$, constraining the attack strength yields learning curves that closely match the early epochs of the curves obtained when the attack strength is allowed to grow freely. Consequently, it suffices to run the experiments with $\gamma = 0$. The adversarial layers are trained using stochastic gradient descent, a batch size of 64 for binary classification and a batch size of 256 for four-class classification. The larger batch size for four-class classification helps accelerate training, as the dataset is larger for this task. The learning rate for training the adversarial layers is set to 0.001 for MNIST, matching the rate used for training the classifier. For FMNIST, as detailed in Section $C.3.5$, we experimented with learning rates of 0.001 and 0.005, ultimately selecting 0.005 due to its superior performance. Similarly, for CIFAR-2, we adopted a higher learning rate of 0.005 for the adversarial layers, compared to the classifier's learning rate of 0.0005. Section $C.3.5$ provides the rationale for these hyperparameter choices and reports the comparative results that motivated the selected learning rates.

C.3.2 Interpreting the Results

Here, we analyze the experimental results; the associated plots are presented in the following Sections C.3.3 and C.3.4 .

C.3.2.1 Vulnerability of Partitioned vs Unpartitioned Classifiers: In the figures presented in Sections C.3.3 and C.3.4, plots that exhibit higher misclassification rates for a given attack strength correspond to more successful adversarial attacks. Across these figures, we observe that introducing a single adversarial block can, in some instances, yield more successful attacks when the perturbations are implemented within intermediate layers of the circuit than when they target the input layer (see Figs. 8.(a), 10.(b), 11.(b), 12, 13.(a), 16, 17, 18.(b), or 19.(b)). This suggests that partitioning and distributing quantum classifiers can increase their vulnerability to adversarial attacks. In a distributed setting, adversarial perturbations can be introduced within intermediate layers of the partitioned classifiers by manipulating the wire cutting or state teleportation procedures, whereas unpartitioned classifiers can only be attacked by perturbing their input states. A second way in which partitioned quantum classifiers are more vulnerable than centralized ones is that an adversary can inject multiple perturbations across their intermediate layers by manipulating multiple wire cutting or state teleportation processes simultaneously.

Comparing the effects of inserting three adversarial blocks versus a single one, we observe that when the attack strength is measured using the (normalized) sum of Hilbert Schmidt distances between the adversarial unitaries implemented within the architecture and the identity operator, single adversarial blocks are often able to achieve a higher misclassification rate at a given attack strength. This, however, depends on how we define the attack strength and would change if we defined it in terms of the (normalized) average of Hilbert Schmidt distances. In such cases, the plots associated with single adversarial blocks would remain unchanged, whereas those corresponding to multiple blocks would often show improved performance, surpassing that of single blocks. This makes sense intuitively: when the attack strength is defined based on the average of Hilbert Schmidt distances, using multiple adversarial blocks generally leads to better outcomes. For clarity, all plots are based on the sum of Hilbert Schmidt distances. However, one can infer how they might differ if the average were used instead.

C.3.2.2 Global vs Local Adversarial Layers: By comparing the figures in Section C.3.3 with those in Section C.3.4, we observe that when the adversarial layers are allowed to act on all qubits, they often perform better than local adversarial gates. However, this is not always the case: in some instances, restricting the adversarial attacks to local qubits can yield more successful attacks. For example, compare Figs. 13 and 17, which correspond to local adversarial attacks, with Fig. 8, which corresponds to global attacks.

C.3.2.3 Effects of the Number of Layers: Figures in Sections C.3.3 and C.3.4 show that adversarial blocks consisting of more layers tend to produce more successful attacks (compare subfigures (a) and (b) in Figs. 12, 21, and 22). Conversely, although deeper classifiers (i.e., classifiers with more layers) are generally expected to be more resilient to adversarial attacks, this is not always observed in practice. For instance, Figs. 10 and 11 illustrate a case where the deeper classifier (Fig. 11) is not more robust.

C.3.3 Global Adversarial layers

Here, we present the result for the case where the adversarial layers act on all qubits. In the following plots, each line represents the average of three runs, with the shaded regions surrounding the lines indicating the variance across these runs. The individual points correspond to the actual data collected from the experiments, and the dotted lines connect these points to illustrate the trends observed. The fluctuations in the plots result from the inherent randomness of stochastic gradient descent and the shuffling of batches at each epoch, which alters the data order used for gradient calculation, causing slight variations in the optimization path and final model parameters.

C.3.3.1 MNIST and FMNIST: In Figures 8 to 11, the plots on the left show the results for the MNIST dataset, while those on the right show the results for the FMNIST dataset. In all these figures, the number of adversarial layers is indicated in the caption for plots corresponding to a single adversarial block. For plots showing the results for multiple blocks of adversarial layers, the legends displays both the position of the adversarial blocks and the number of layers in each block.

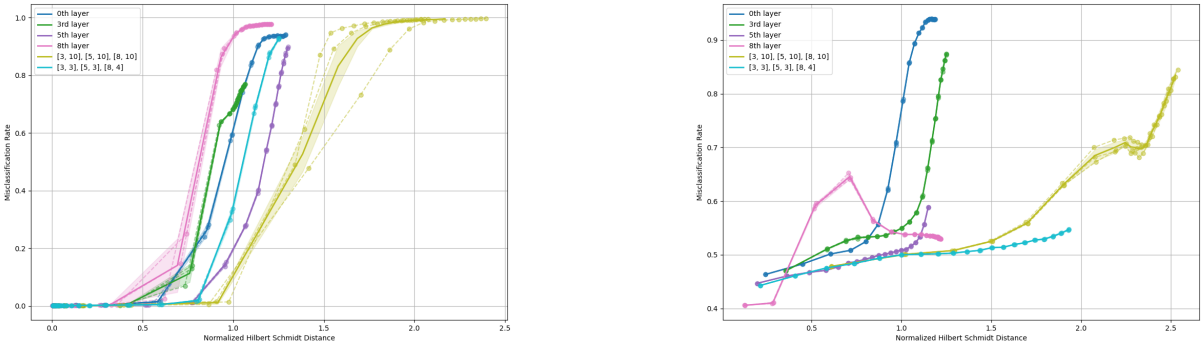

(a) (b)

Figure 8: These plots depict misclassification rate (y-axis) against attack strength (x-axis) for a binary classifier, where an adversarial block consisting of 10 layer is incorporated into a model with 10 existing layers. The plots on the left show the results for the MNIST dataset, with the plots on the right displaying the results for the FMNIST dataset. The performance of these adversarial blocks is compared with two cases where multiple adversarial blocks are inserted at different depths within the architecture. In the first case, the total number of adversarial layers is 10, whereas in the second case, there are 30 adversarial layer, organized into three blocks with 10 layers each. The attack strength is determined by the sum of Hilbert Schmidt distances between the unitary operators the adversarial blocks induce and the identity operator. In the legend, each plot labeled '$q-$th layer' corresponds to an adversarial block located between the $q-$th and $(q+1)-$th layers of the classifier. In contrast, plots labeled '$[q_1, r_1], [q_2, r_2], [q_3, r_3]$' represent three adversarial blocks inserted between the q_1-th and $(q_1+1)-$th layers, the q_2-th and $(q_2+1)-$th layers, and the q_3-th and $(q_3+1)-$th layers, where the first, second, and third block consist of r_1, r_2, and r_3 adversarial layers, respectively. Note that the maximum Hilbert Schmidt distance between two unitary operators is $\sqrt{2}$. Consequently, the sum of the distances between three unitary perturbation operators and the identity operator is at most $3\sqrt{2}$.

(a) (b)

Figure 9: Comparing the effects of inserting an adversarial block consisting of 10 layers into a binary classifier with 20 existing layers versus incorporating three adversarial blocks. In the multiple-block settings, the number of layers for each block is detailed in the legends, where the legends are organized similarly to that of Fig. 8.

(a) (b)

Figure 10: Comparing the effects of inserting an adversarial block consisting of 10 layers into a four-class classifier with 20 existing layers versus incorporating three adversarial blocks.

(a) (b)

Figure 11: Comparing the effects of inserting an adversarial block consisting of 10 layers into a four-class classifier with 40 existing layers versus incorporating three adversarial blocks.

C.3.3.2 CIFAR-2: The left plot in Figure 12 illustrates the effects of modifying an 80-layer quantum classifier by inserting a 10-layer adversarial block within its layers, while the right plot shows the results when a 40-layer adversarial block is inserted. For the cases where multiple blocks of adversarial layers are inserted, the legends specifies both the insertion depth and the number of layers in each added block.

(a) (b)

Figure 12: Impact of inserting adversarial blocks into an 80-layer classifier trained on CIFAR-2. The left plot shows the effect of adding a 10-layer block, while the right plot shows the effect of adding a 40-layer block. In contrast to Figure 8, where the left and right plots correspond to classifiers trained on MNIST and FMNIST, both plots here present results for a classifier trained on CIFAR-2.

C.3.4 Local Adversarial layers

C.3.4.1 MNIST and FMNIST: The results presented here correspond to the case where the adversarial gates act on a local set of qubits, specifically qubits $3, 4$ and 5 for Figures 13 to 16 and qubits $5, 6, 7$ and 8 for Figures 17 to 20 (See Figure 7's caption for the qubit numbering scheme used in our experiments). In Figs. 13–20, the left-hand plots correspond to the MNIST dataset, and the right-hand plots correspond to the FMNIST dataset.

(a) (b)

Figure 13: Comparing the effects of inserting an adversarial block consisting of 10 layers into a binary classifier with 10 existing layers versus incorporating three adversarial blocks. In contrast to Fig. 8, where the adversarial layers act on all qubits, here the adversarial layers act only on qubits number $3, 4$ and 5.

(a) (b)

Figure 14: Comparing the effects of inserting an adversarial block consisting of 10 layers into a binary classifier with 20 existing layers versus incorporating three adversarial blocks. Unlike Fig. 9, where the adversarial layers act on all qubits, here the adversarial layers act only on qubits number $3, 4$ and 5.

(a) (b)

Figure 15: Comparing the effects of inserting an adversarial block consisting of 10 layers into a four-class classifier with 20 existing layers versus incorporating three adversarial blocks. Contrary to Fig. 10, where the adversarial layers act on all qubits, here the adversarial layers act only on qubits number $3, 4$ and 5.

(a) (b)

Figure 16: Comparing the effects of inserting an adversarial block consisting of 10 layers into a four-class classifier with 40 existing layers versus incorporating three adversarial blocks. In contrast to Fig. 11, where the adversarial layers act on all qubits, here the adversarial layers act only on qubits number $3, 4$ and 5.

(a) (b)

Figure 17: Comparing the effects of inserting an adversarial block consisting of 10 layers into a binary classifier with 10 existing layers versus incorporating three adversarial blocks. Unlike Fig. 8, where the adversarial layers act on all qubits, here the adversarial layers act only on qubits number $5, 6, 7$ and 8.

(a) (b)

Figure 18: Comparing the effects of inserting an adversarial block consisting of 10 layers into a binary classifier with 20 existing layers versus incorporating three adversarial blocks. In contrast to Fig. 9, where the adversarial layers act on all qubits, here the adversarial layers act only on qubits number $5, 6, 7$ and 8.

(a) (b)

Figure 19: Comparing the effects of inserting an adversarial block consisting of 10 layers into a four-class classifier with 20 existing layers versus incorporating three adversarial blocks. Contrary to Fig. 10, where the adversarial layers act on all qubits, here the adversarial layers act only on qubits number $5, 6, 7$ and 8.

(a) (b)

Figure 20: Comparing the effects of inserting an adversarial block consisting of 10 layers into a four-class classifier with 40 existing layers versus incorporating three adversarial blocks. In contrast to Fig. 11, where the adversarial layers act on all qubits, here the adversarial layers act only on qubits number $5, 6, 7$ and 8.

C.3.4.2 CIFAR-2: Fig. 21 below shows the effect of inserting local adversarial gates acting on qubits $3, 4$ and 5 whereas Fig. 22 corresponds to the case where the adversarial gates act on qubits $5, 6, 7$ and 8.

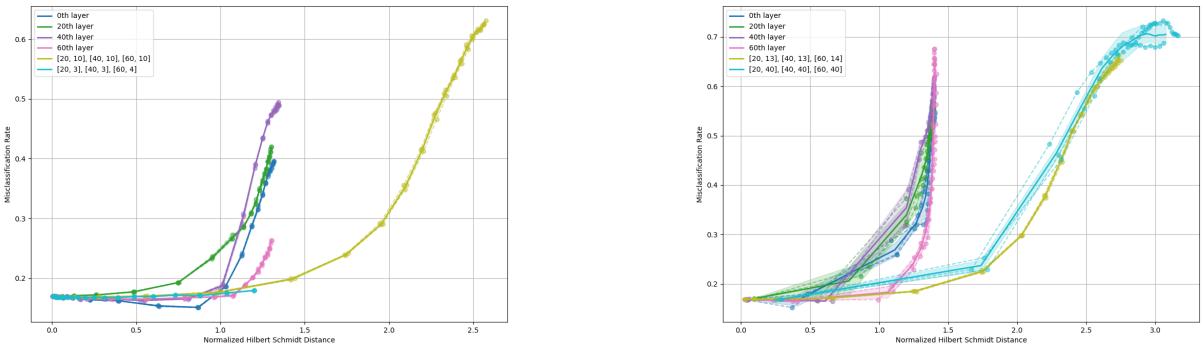

(a) (b)

Figure 21: Impact of inserting local adversarial blocks into an 80-layer classifier trained on CIFAR-2. The left plot shows the effect of adding a 10-layer block, while the right plot shows the effect of adding a 40-layer block. The adversarial layers act only on qubits number $3, 4$ and 5. For the cases where multiple adversarial blocks are inserted, the legends specifies the insertion depth and the number of layers in each added block. In contrast to Figures 13 to 20 where the left and right plots correspond to classifiers trained on MNIST and FMNIS, both plots here present results for a classifier trained on CIFAR-2.

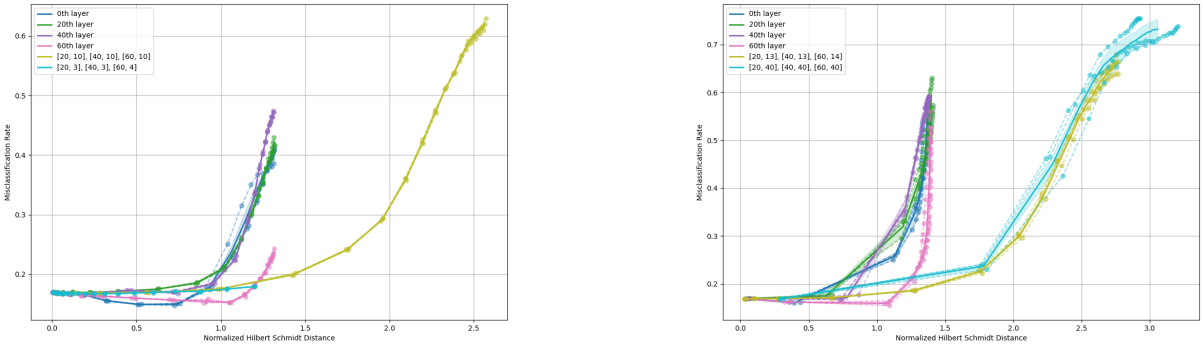

(a) (b)

Figure 22: Effect of inserting local adversarial blocks into an 80-layer classifier trained on CIFAR-2. The left plot shows the effect of adding a 10-layer block, while the right plot shows the effect of adding a 40-layer block. The adversarial layers act only on qubits number $5, 6, 7$ and 8. In contrast to Figures 13 to 20, where the left and right plots correspond to classifiers trained on MNIST and FMNIS, both plots here present results for a classifier trained on CIFAR-2.

C.3.5 Rationale for Selected Hyperparameters

This section details the empirical results underpinning our selection of hyperparameters, in particular the learning rate and γ.

C.3.5.1 Learning Rates: For MNIST, we employ the same learning rate for training both the classifier and the adversarial layers. As demonstrated in Figures 23 and 24, higher learning rates are adopted for FMNIST and CIFAR-2 because they result in improved adversarial performance.

Figure 23: Effects of inserting an adversarial block consisting of 10 layers into a binary classifier with 10 existing layers trained on FMNIST versus incorporating three adversarial blocks. The left plot shows the results when the adversarial layers are trained with a learning rate of 0.001, whereas the right plot corresponds to a learning rate of 0.005, which yields better adversarial performance on FMNIST.

Figure 24: Effects of inserting an adversarial block consisting of 10 layers into a binary classifier with 80 existing layers trained on CIFAR-2 versus incorporating three adversarial blocks. The left plot shows the results when the adversarial layers are trained with a learning rate of 0.001, whereas the right plot corresponds to a learning rate of 0.005, which yields better adversarial performance on CIFAR-2.

C.3.5.2 Constraining the Attack Strength: Figures 25 to 28 demonstrate that when the attack strength is constrained by increasing the parameter γ in (35), the attack scenarios that are more successful than others before the constraint is applied remain more successful afterward. For example, in Figure 25, which illustrates the effect of adding adversarial blocks to a 10-layer classifier trained on MNIST for binary classification, the block inserted between the 8th and 9th layer of the classifier is more successful than the other adversarial perturbations in the leftmost subfigure, and it continues to outperform them as we move from the leftmost to the rightmost subfigure, increasing γ and the attack constraint. Figures 25 to 28 further show that the plots corresponding to more constrained attacks resemble the early-epoch behavior of the plots obtained when the attacks are unconstrained. Therefore, it is sufficient to study the attacks in the unconstrained setting with $\gamma = 0$.

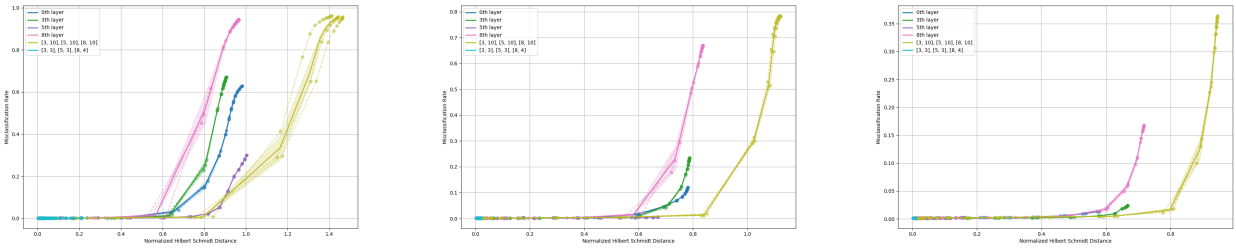

Figure 25: Effect of constraining the attack strength when adversarial layers are incorporated into a model with 10 existing layers trained on MNIST for binary classification. The leftmost subfigure imposes the weakest constraint on the strength, which gradually increases as we move from left to right. The parameter γ is set to $0.5, 1$, and 1.5 in the subfigures from left to right.

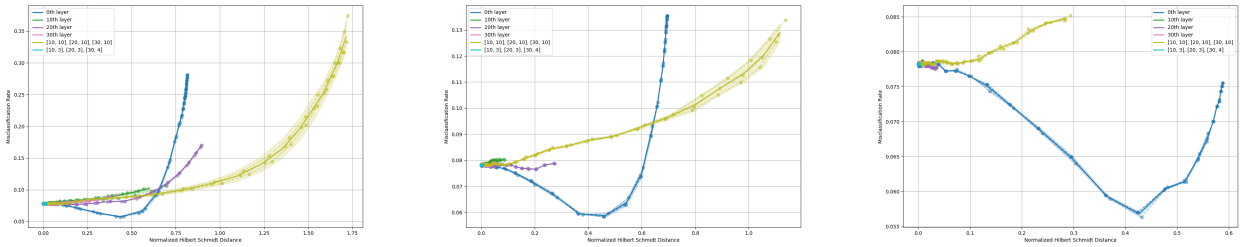

Figure 26: Effect of constraining the attack strength when adversarial layers are incorporated into a model with 40 existing layers trained on MNIST for four-class classification. The parameter γ is set to $0.5, 1$, and 1.5 in the subfigures from left to right.

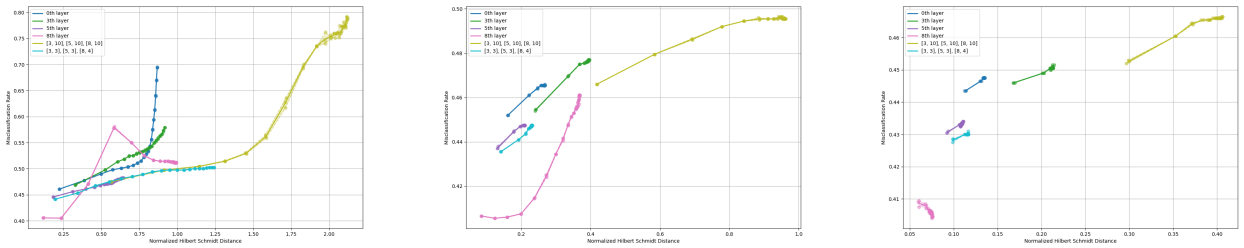

Figure 27: Effect of constraining the attack strength when adversarial layers are incorporated into a model with 10 existing layers trained on FMNIST for binary classification. The parameter γ is set to $0.1, 0.5$ and 1 in the subfigures from left to right.

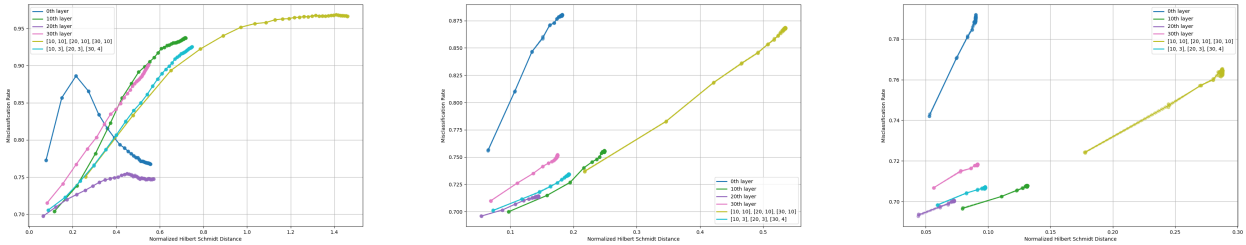

Figure 28: Effect of constraining the attack strength when adversarial layers are incorporated into a model with 40 existing layers trained on FMNIST for four-class classification. The parameter γ is set to $0.1, 0.5$ and 1 in the subfigures from left to right.

C.4 Evaluating our Theoretical Bound

Theorem 6.3 provides a probabilistic bound on $|y_k(\sigma) - \hat{y}_k(\sigma)|$, where $\hat{y}_k(\sigma)$ and $y_k(\sigma)$ denote the probabilities of assigning label k to an input sample σ before and after an adversarial attack, respectively. This result is particularly useful in the binary-classification setting. In that case, once we know the pre-attack probabilities assigned to the two labels, the bound in the theorem allows us to determine whether an adversarial attack can flip the classifier's predicted label for σ. To assess whether Theorem 6.3 is useful in practice, we must determine how tight the bound it provides actually is. The experiments below are designed to evaluate this.

In Figs. 29-33, the blue plots show how the average probability assigned to the true class evolves as we increase the strength of the adversarial attack. Specifically, for each input sample σ, we take k to be its true label, and then compute the mean of $\hat{y}_k(\sigma)$ over all samples in the test dataset. Each blue dot on the plots corresponds to a training epoch, for which both the average probability and the strength of the attack are computed at the end of the epoch. The shaded light-blue region

shows ± 1 standard deviation. The orange, red, and purple plots show the upper and lower bounds predicted by Theorem 6.3 for $\hat{y}_k(\sigma)$ for a given strength of attack, corresponding to confidence levels of $90\%, 95\%$, and 99%, respectively. Figs. 29 and 30 showing 10- and 20-layer classifiers, depict results for MNIST, while Figs. 31 and 32 correspond to 10- and 20-layer classifiers trained on FMNIST, and Fig. 33 corresponds to an 80-layer classifier trained on CIFAR-2. All classifiers are trained for binary classification. These figures show that for MNIST and FMNIST, the lower bounds provided by Theorem 6.3, corresponding to confidence levels of 90% and 95%, are in most cases close to the actual probabilities assigned to the true class and predict them well. However, for CIFAR-2, the bounds provided by Theorem 6.3 can become loose as the strength of the attack increases. Nonetheless, this demonstrates that, while the bounds may occasionally loosen, Theorem 6.3 provides useful predictions in the majority of cases. For CIFAR-2, the lower bounds remain tight relative to the actual probabilities when the attack strength is low. Given that increasing attack strength typically reduces stealthiness, these findings highlight the practical utility of our bound for stealthy adversarial attacks.

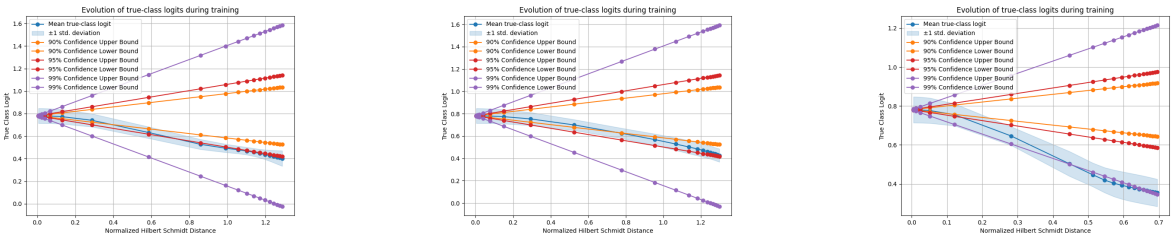

(a) (b) (c)

Figure 29: Evolution of the average probability assigned to the true class for a 10-layer quantum classifier trained on MNIST as we increase the strength of the attack, where the strength is measured in terms of the normalized Hilbert Schmidt distance. Subfigure (a) corresponds to a 10-layer adversarial block inserted before the 1st layer of the classifier, subfigure (b) to a 10-layer adversarial block inserted after the 5th layer and before the 6th layer, while subfigure (c) corresponds to inserting three 10-layer adversarial blocks after layers 3, 5, and 8 of the classifier. In subfigures (a) and (b), we observe that the lower bounds provided by Theorem 6.3, corresponding to confidence levels of 90% and 95%, are close to the actual probabilities assigned to the true class and predict them well. However, in subfigure (c), the actual probabilities are lower than the bounds predicted at the 90% and 95% confidence levels and are closer to the bound predicted at the 99% confidence level by Theorem 6.3.

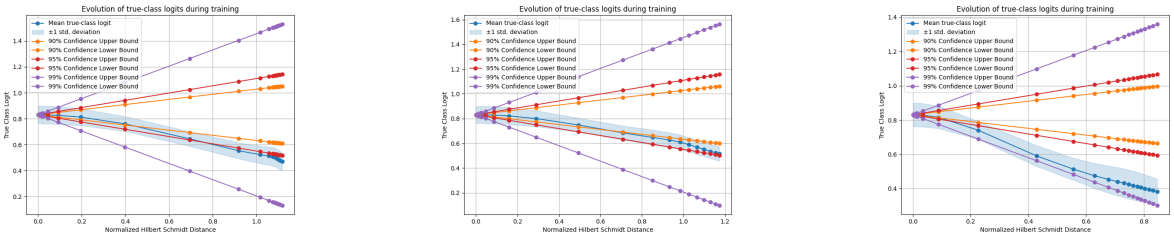

(a) (b) (c)

Figure 30: Evolution of the average probability assigned to the true class for a 20-layer quantum classifier trained on MNIST as we increase the strength of the attack. Subfigure (a) corresponds to a 10-layer adversarial block inserted before the 1st layer of the classifier, subfigure (b) to a 10-layer adversarial block inserted after the 10th layer and before the 11th layer, while subfigure (c) corresponds to inserting three 10-layer adversarial blocks after layers 5, 10, and 15.

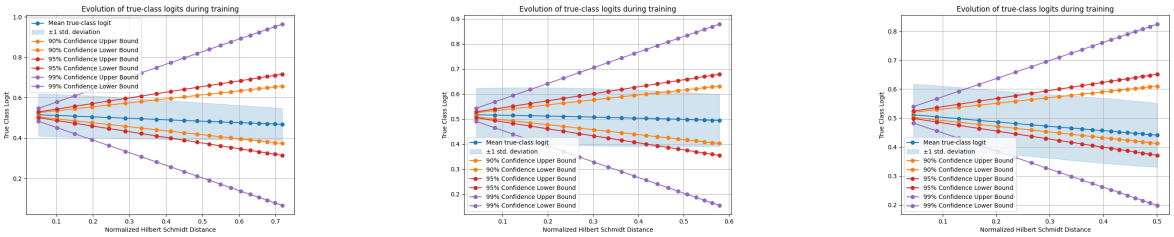

(a) (b) (c)

Figure 31: Evolution of the average probability assigned to the true class for a 10-layer quantum classifier trained on FMNIST as we increase the strength of the attack. Subfigure (a) corresponds to a 10-layer adversarial block inserted before the 1st layer of the classifier, subfigure (b) to a 10-layer adversarial block inserted after the 5th layer and before the 6th layer, while subfigure (c) corresponds to inserting three 10-layer adversarial blocks after layers 3, 5, and 8.

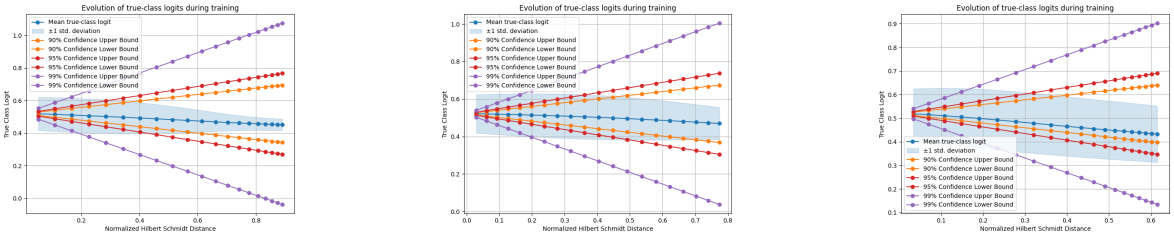

(a) (b) (c)

Figure 32: Evolution of the average probability assigned to the true class for a 20-layer quantum classifier trained on FMNIST as we increase the strength of the attack. Subfigure (a) corresponds to a 10-layer adversarial block inserted before the 1st layer of the classifier, subfigure (b) to a 10-layer adversarial block inserted after the 10th layer and before the 11th layer, while subfigure (c) corresponds to inserting three 10-layer adversarial blocks after layers 5, 10, and 15.

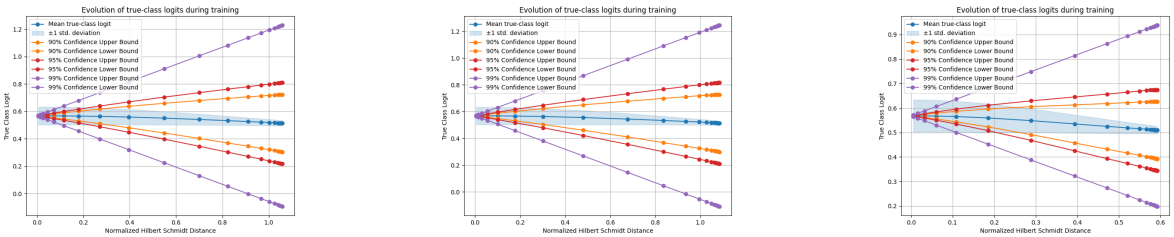

(a) (b) (c)

Figure 33: Evolution of the average probability assigned to the true class for a 80-layer quantum classifier trained on CIFAR-2 as we increase the strength of the attack. Subfigure (a) corresponds to a 10-layer adversarial block inserted before the 1st layer of the classifier, subfigure (b) to a 10-layer adversarial block inserted after the 40th layer and before the 41th layer, while subfigure (c) corresponds to inserting three 10-layer adversarial blocks after layers 20, 40, and 60.